Available online at www.sciencedirect.com

ScienceDirect

Advances in Space Research 75 (2025) 1597–1615

ADVANCES IN SPACE RESEARCH (a COSPAR publication)

www.elsevier.com/locate/asr

Simplified Earth infrared and albedo coefficient models for spacecraft thermal analysis based on the CERES data products

Kaname Sasaki

DLR German Aerospace Center, Institute of Space Systems, Robert-Hooke-Str. 7, 28359 Bremen, Germany

Received 29 June 2024; received in revised form 7 November 2024; accepted 9 November 2024
Available online 19 November 2024

Abstract

For Earth-orbiting spacecraft, infrared flux and albedo flux from the Earth surface have a major impact on their thermal behavior. Earth infrared flux, also known as Outgoing Longwave Radiation (OLR), and the albedo coefficient are often evaluated as a uniform value in the spacecraft thermal analysis. However, in reality, these values exhibit complex variation over area and time. In this study, we propose simplified models for describing the OLR and albedo coefficient distributions, based on the measurement-based dataset compiled by Clouds and the Earth's Radiant Energy System (CERES) project. The model consists of spherical harmonics and trigonometric functions for representing the spatial distribution and temporal variation, respectively. The model parameters are calculated to minimize the root mean square error (RMSE) between the model and the CERES dataset. The constructed models are employed to calculate the infrared and albedo flux in various types of orbits. These results are then compared to the flux values calculated by using the CERES dataset. The evaluation demonstrates that the model represents the overall spatial and temporal trend of the infrared and albedo flux. Additionally, by incorporating ± 1 RMSE between the model and CERES dataset as the model uncertainties, hot and cold environments can be formulated to account for the effect of the local variations of the OLR and albedo coefficient.

Keywords: Spacecraft thermal analysis; albedo; Earth infrared; OLR; spherical harmonics; CERES

1. Introduction

1.1. Conventional methods

Thermal environmental conditions are the critical design drivers for the spacecraft thermal control system. Direct solar flux is normally the most significant external heat source for a spacecraft. However, for a low Earth orbit (LEO) satellite, infrared flux from the Earth surface, known as Outgoing Longwave Radiation (OLR), and reflected solar flux, known as albedo flux, are also important factors. Intensity of infrared and albedo flux received by a satellite depends on various parameters, such as satellite position, orientation, solar irradiance, direction of the solar flux, Earth surface properties and temperatures, and cloud coverage. Since it is impractical to evaluate every thermal environment, which the satellite could encounter within its lifetime, the typical approach is to estimate the hot and cold worst-case thermal environmental conditions and assess the design feasibility. For such worst-case thermal analyses, the OLR and albedo coefficient are normally assumed to be uniform values for the simplicity. However, as the uniform values cannot represent the variable characteristics of the OLR and albedo coefficient within each analysis case, this evaluation approach include some fundamental drawbacks. For example, if the selected values account for the short-term maximum and minimum values, the resulting thermal environment becomes too conservative. Conversely, if the

E-mail address: Kaname.Sasaki@dlr.de

https://doi.org/10.1016/j.asr.2024.11.024
0273-1177/

Nomenclature

$\alpha(\theta,\varphi,t)$	albedo coefficient as a function of latitude, longitude, and time
$\epsilon(\theta,\varphi,t)$	Earth infrared flux as a function of latitude, longitude, and time
α_{ijk}	albedo coefficient value at the grid point (i,j) and time k
ϵ_{ijk}	Earth infrared flux value at the grid point (i,j) and time k
θ	colatitude, $0^\circ \leqslant \theta \leqslant 180^\circ$
φ	longitude, $0^\circ \leqslant \varphi \leqslant 360^\circ$
$Y_{l,m}$	spherical harmonics of degree l and order m
$P_{n,3}$	Legendre polynomial of order n
$P_{n,3}^{(m)}$	m-th derivative of n-th order Legendre polynomial
$\widetilde{P}_{n,3,m}$	normalized associated Legendre function of order n and degree m
$\widetilde{S}_n^m(t_0,t_1)$	definite integral of the normalized associated Legendre function from t_0 to t_1
i	index for colatitude, $0 \leqslant i \leqslant 179$
j	index for longitude, $0 \leqslant j \leqslant 359$
k	index for time
a_{lmk}	spherical harmonics coefficient of albedo coefficient
e_{lmk}	spherical harmonics coefficient of Earth infrared flux
$\mathrm{MSE}_{\alpha,k}$	spatially normalized squared error of albedo coefficient at time k
$\mathrm{MSE}_{\epsilon,k}$	spatially normalized squared error of Earth infrared flux at time k
MSE_{α}	mean squared error of albedo coefficient
MSE_{ϵ}	mean squared error of Earth infrared flux
RMSE_{α}	root mean squared error of albedo coefficient
RMSE_{ϵ}	root mean squared error of Earth infrared flux
G_{on}	extraterrestrial radiation incident on the plane normal to the radiation, $\mathrm{W/m^2}$
G_{sc}	Solar constant, $1361.1\,\mathrm{W/m^2}$ (Gueymard (2018))
R	Earth radius based on WGS84 equator, 6378.137 km (NGA.STND (2014))
JD	Julian date
δ_{sun}	declination of the Sun
α_{sun}	right ascension of the Sun
DOY	day of year, DOY = 1 corresponds to January 1
λ	rotation angle between the geocentric equatorial (IJK) coordinate system and the Earth-centered Earth-fixed (ECEF) coordinate system
S	distance between a satellite surface and a facet of the Earth surface
Θ_0	angle between the satellite surface normal and a line connecting the satellite surface and the differential area on the Earth surface
Θ_1	angle between the Earth surface normal and a line connecting the satellite surface and the differential area on the Earth surface
Φ	solar zenith angle
T_{sidereal}	sidereal day, 86164.0905 s (Vallado and McClain (2013))
R_{ADM}	anisotropic factor based on the Angular Distribution Model (ADM)
σ	Stefan–Boltzmann constant, $5.6693 \times 10^{-8}\,\mathrm{W/m^2K^4}$ (Panczak et al. (2020))
T_∞	deep space temperature, 2.73 K (Panczak et al. (2020))
C_{node}	node heat capacity of the single-node thermal model, J/K
α_{s}	absorptivity of the single-node thermal model surface
ϵ_{s}	emissivity of the single-node thermal model surface
T_{node}	node temperature of the single-node thermal model, K
$\dot{Q}_{\mathrm{sun}}$	incident solar flux on the single-node thermal model surface, W
$\dot{Q}_{\mathrm{ir}}$	incident infrared flux on the single-node thermal model surface, W
$\dot{Q}_{\mathrm{al}}$	incident albedo flux on the single-node thermal model surface, W

selected values are based on the time-averaged values, the short-term critical conditions cannot be considered in the thermal analysis.

One of the most common methods for specifying the worst hot and cold parameters is described in the National Aeronautics and Space Administration (NASA) technical memorandum by Anderson et al. (2001). Using the tables and correction factors given in this report, a pair of OLR and albedo coefficient values can be selected based on the orbit inclination, thermal time constant, and the surface properties information. This parameter selection process was also implemented as a computer program called STEM (Spacecraft Thermal Environment Model), as presented by Justus et al. (2001). As a different approach, ECSS-E-ST-10-04C (2008) presents the OLR and albedo coefficient models, which are variable over time and area. Those models were proposed by Knocke et al. (1988) for studying the radiation pressure effect on an Earth-orbiting spacecraft, and the models consist of the Legendre polynomials and the trigonometric functions for representing the spatial and time variation. The model parameters are calculated from the study results by Stephens et al.

(1981), where the Earth radiation budgets were evaluated based on the satellite observation data in 1960s and 1970s. These models have been widely used for evaluating the radiation pressure effect on the spacecraft orbit, and some applications on the spacecraft thermal analysis, such as a study by Fu et al. (2024), can be found as well.

Recent studies on the radiation pressure effect and the spacecraft thermal analysis utilize the measurement-based datasets, compiled by NASA's Clouds and the Earth's Radiant Energy System (CERES) project. Vielberg and Kusche (2020) proposed a Earth radiation pressure model based on the CERES data products and applied the model to GRACE (Gravity Recovery and Climate Experiment) data for validation. Also, Reynerson and Hakuba (2023) analyzed albedo and longwave radiation pressure, and performed comparison between the results based on the CERES data products and the models by Knocke et al. (1988). In the field of spacecraft thermal analysis, Green and Peyrou-Lauga (2015) and Peyrou-Lauga (2017a,b, 2022) developed a dedicated tool at European Space Agency (ESA) for evaluating OLR and albedo flux based on the CERES data product. With this tool, it is possible to calculate the effective OLR and albedo coefficient for a given position in the orbit. González-Bárcena et al. (2021, 2022a) performed a review on the derivation method of the worst thermal environmental conditions for LEO satellites by using the CERES data products. In addition to Earth-orbiting spacecrafts, the thermal effect of the albedo and OLR fluxes are important aspect for a balloon borne system as well. Borden et al. (2017) performed the thermal analysis for the fine pointing stage of a balloon based imaging system. In this analysis, the albedo flux is specified based on the CERES data. Also, González-Llana et al. (2018) and González-Bárcena et al. (2020, 2022b) utilized the CERES data to specify the environmental conditions for the flight area of the long duration balloon mission.

These studies indicate that the openly available datasets encourage researchers in this field to conduct measurement-based OLR and albedo flux evaluation for Earth-orbiting spacecraft and balloon borne systems. On the other hand, utilizing such extensive dataset and accurately defining the applicable thermal environment is not straightforward. In this study, we propose simplified models of the OLR and albedo coefficient distribution, which can be applied to the spacecraft thermal analysis. The models are constructed based on the spherical harmonics expansion with time-variant coefficients, and the model parameters are calculated to minimize the root mean square error (RMSE) from the CERES data products. In this way, the model can be determined by limited number of parameters and applicable to different orbits and seasons.

1.2. Clouds and Earth Radiant Energy System (CERES)

Before describing the modeling and evaluation method, we will introduce the CERES project and the utilized data products. Satellite-based observations of the Earth's radiation budget (ERB) are the essential information for understanding the Earth's climate system, especially the flow of energy. The CERES project utilizes the measurements from the CERES instruments and other data sources to provide a global record of the ERB (Wielicki et al. (1996)). The CERES instrument is a scanning radiometer with three spectral channels: a shortwave channel for 0.3–5 μm range, a total channel for 0.3–200 μm range, and either a window channel for 8–12 μm range or a longwave channel for 5–35 μm range. The CERES instruments are onboard multiple satellites, including PFM on the tropical rainfall measuring mission (TRMM) launched in November 1997, FM1 and FM2 on Terra launched in December 1999, FM3 and FM4 on Aqua in May 2002, FM5 on Suomi National Polar-orbiting Partnership (S-NPP) in October 2011, and FM6 on NOAA-20 launched in November 2017. Except for TRMM, those satellites were inserted to the Sun synchronous orbit (SSO), which allows the global observation coverage (Loeb et al. (2018, 2023)).

The CERES measurement data is processed by the CERES project team, and different types of processed data products are publicly available via the NASA Langley Research Center CERES ordering tool at https://ceres.larc.nasa.gov/data/. For the spacecraft thermal analysis, the major interest is on the spatial and temporal distribution of the heat fluxes from the top of atmosphere (TOA). The original CERES instrument output values are converted to the unfiltered radiances, considering the instrument calibration and sensor spectral responses. This unfiltered radiances, which are the arrived radiances at the sensor position and orientation, are converted to the TOA fluxes by using Angular Distribution Models (ADMs), where the latest methodology of ADMs is described in Su et al. (2015a,b). As indicated in the orbit information, the local time frame of the CERES measurement is constrained, and it is difficult to capture the variable characteristics of the Earth radiation within each day. Also, daily data from each satellite can contain some missing data regions. In order to overcome this limitation, SYN1deg data products incorporate the data from geostationary satellites as described in Doelling et al. (2013, 2016), and provide up to 1-hourly data for more than 20 years. In this study, the daily version of SYN1deg data product, SYN1deg-Day Ed4.1 (NASA/LARC/SD/ASDC (2017)), is used as the reference distribution of OLR and albedo coefficient, in order to capture the spatial and seasonal variation of the heat fluxes.

As an example, Fig. 1 and 2 show the OLR and the albedo coefficient distributions, extracted from the CERES SYN1deg-Day Ed4.1 product. As shown in the figures, the OLR and albedo coefficient distributions are primarily dependent on latitude with additional seasonal characteristics. The OLR values are generally higher in the equator region and lower near the poles. Conversely, the albedo coefficient display an opposite trend, with higher values observed at higher latitudes. In some seasons, the albedo

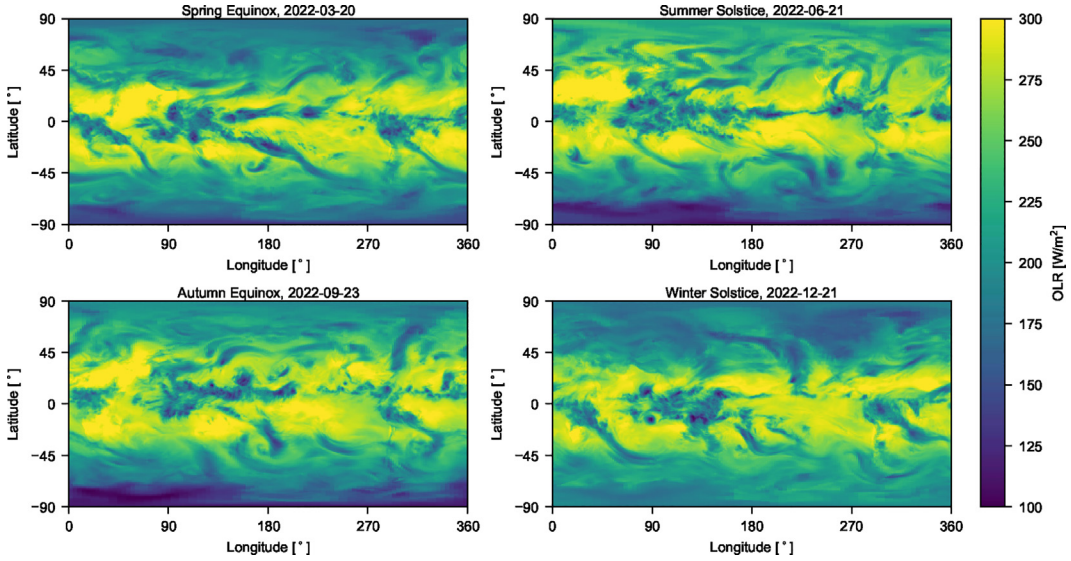

Fig. 1. OLR distributions for different seasons in 2022. The data is extracted from the CERES SYN1deg-Day Ed4.1 product.

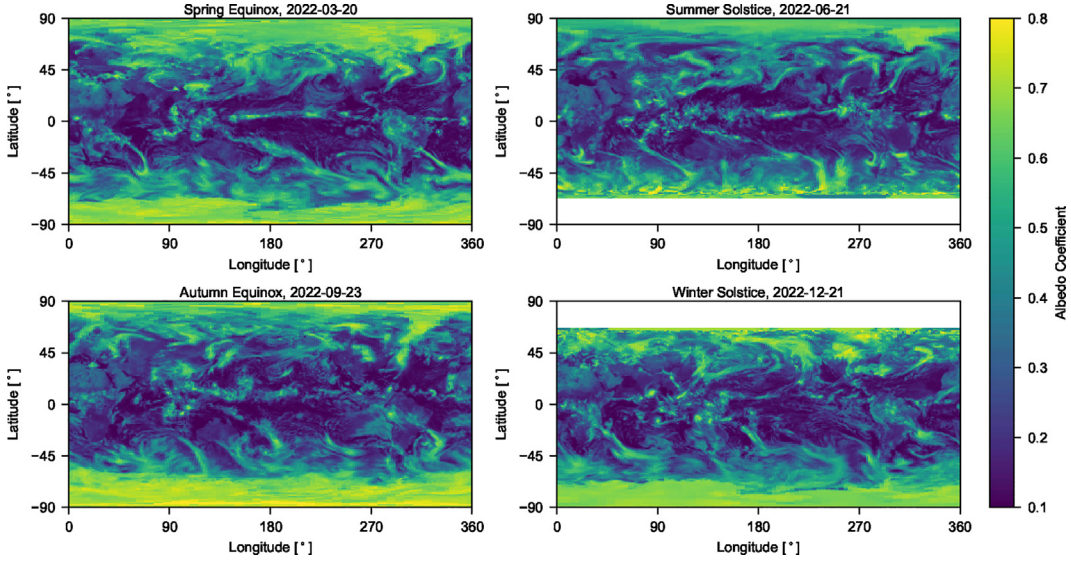

Fig. 2. Albedo coefficient distributions for different seasons in 2022. The data is extracted from the CERES SYN1deg-Day Ed4.1 product.

coefficient data is missing near the polar regions. Around the summer solstice, the albedo coefficient is physically expected to be high at the south pole region. However, due to the polar night period, there is no measured albedo flux and no corresponding albedo coefficient. Similarly, there are no measured albedo values for north pole region around winter solstice. In the following sections, details of the modeling method and its performance are described.

2. OLR and albedo coefficient model

2.1. Modeling concept

The distributions of OLR and albedo coefficient are considered to be functions of a location on a spherical surface and time. In order to describe the spatial variation and temporal variation, the considered form is a product of spherical harmonics and another function of time.

$$\epsilon(\theta,\varphi,t) \simeq \sum_{l,m} e_{lm}(t) Y_{l,m}(\theta,\varphi), \tag{1}$$

$$\alpha(\theta,\varphi,t) \simeq \sum_{l,m} a_{lm}(t) Y_{l,m}(\theta,\varphi). \tag{2}$$

In these formulas, ϵ and α represent the OLR and albedo coefficient as functions of colatitude θ, longitude φ, and time t (Fig. 3). The right sides of the equations are the spherical harmonics expansion of the OLR and albedo coefficient distributions. The coefficients e_{lm} and a_{lm} are time-variant.

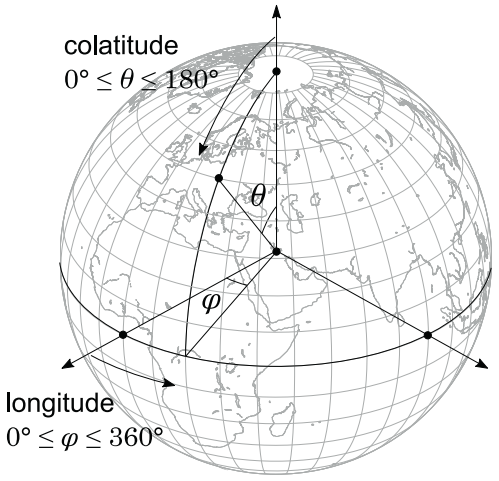

Fig. 3. Utilized coordinate parameters for describing the OLR and albedo coefficient distributions.

2.2. Spherical harmonics

In the later discussions, we utilize spherical harmonics and their specific features, to expand the OLR and albedo coefficient distributions. In this section, related spherical harmonics definitions and equations are summarized. The used spherical harmonics are real and unity-normalized form as shown in Eqs. (3)–(5). Following the notations in Atkinson and Han (2012), $P_{n,3}$ is the n-th order Legendre polynomial, and $P_{n,3}^{(m)}$ is the m-th derivative of the n-th order Legendre polynomial.

$$Y_{n,m}(\theta,\varphi)=\sqrt{\frac{\left(n+\frac{1}{2}\right)(n-m)!}{\pi(n+m)!}}(\sin\theta)^m P_{n,3}^{(m)}(\cos\theta)\cos(m\varphi), \quad (3)$$

for $m>0$.

$$Y_{n,0}(\theta,\varphi)=\sqrt{\frac{n+\frac{1}{2}}{2\pi}}P_{n,3}(\cos\theta), \text{for } m=0. \quad (4)$$

$$Y_{n,m}(\theta,\varphi)=\sqrt{\frac{\left(n+\frac{1}{2}\right)(n-|m|)!}{\pi(n+|m|)!}}(\sin\theta)^{|m|} P_{n,3}^{(|m|)}(\cos\theta)\sin(|m|\varphi), \quad (5)$$

for $m<0$.

The CERES data products are available in tabular form and each value corresponds to a latitude-longitude gridded area of the Earth surface. To specify spherical harmonics parameters, the integral of the spherical harmonics in a gridded area is required. The surface integral of the spherical harmonics over a latitude-longitude gridded area is given by

$$\begin{aligned}&\int_{\theta_0}^{\theta_1}\int_{\varphi_0}^{\varphi_1} Y_{n,m}(\theta,\varphi)dS\\ &=\tfrac{1}{\sqrt{\pi}}\int_{\theta_0}^{\theta_1}\widetilde{P}_{n,3,m}(\cos\theta)\sin\theta d\theta\int_{\varphi_0}^{\varphi_1}\cos m\varphi d\varphi\\ &=\tfrac{1}{\sqrt{\pi}}\overline{S}_n^m(t_1,t_0)\left[\tfrac{1}{m}\sin(m\varphi)\right]_{\varphi_0}^{\varphi_1},\end{aligned} \quad (6)$$

where the normalized associated Legendre functions in three dimensions, and the definite integral of the normalized associated Legendre function are defined by the following formulas.

$$\widetilde{P}_{n,3,m}(t)=\left[\frac{\left(n+\frac{1}{2}\right)(n-m)!}{(n+m)!}\right]^{\frac{1}{2}}\left(1-t^2\right)^{\frac{m}{2}}P_{n,3}^{(m)}(t), \quad (7)$$

$$\overline{S}_n^m(t_0,t_1)=\int_{t_0}^{t_1}\widetilde{P}_{n,3,m}(t)dt, \quad (8)$$

$$\cos\theta_0=t_0,\ \cos\theta_1=t_1,\ -1\leqslant t_0,t_1\leqslant 1. \quad (9)$$

The normalized associated Legendre function and its integral are calculated by the recurrence relations as described in Paul (1978) and DiDonato (1982). Those recurrence relations are used to calculate the spherical harmonics parameters in the next section.

2.3. Parameter estimation

To determine the spherical harmonics parameters, we define the squared error between the model and the CERES data on a specific date as shown in Eqs. (10) and (11). $1/4\pi$ is the normalization factor for the integral over the entire sphere. l and m are the degree and order of the spherical harmonics, respectively. The parameter e_{lmk} and a_{lmk} are the spherical harmonics coefficients of the OLR and albedo coefficient for the l-th degree, m-th order, and k-th time stamp.

$$\mathrm{MSE}_{\epsilon,k}=\frac{1}{4\pi}\int_{\mathbb{S}^2}\left(\epsilon(\theta,\varphi,t_k)-\sum_{l=0}^{L}\sum_{m=-l}^{l}e_{lmk}Y_{l,m}\right)^2 dS, \quad (10)$$

$$\mathrm{MSE}_{\alpha,k}=\frac{1}{4\pi}\int_{\mathbb{S}^2}\left(\alpha(\theta,\varphi,t_k)-\sum_{l=0}^{L}\sum_{m=-l}^{l}a_{lmk}Y_{l,m}\right)^2 dS. \quad (11)$$

The reference data used for modeling is SYN1deg-Day Ed4.1, which is the $1^\circ\times1^\circ$ regional and daily averaged TOA fluxes, between March 1, 2000 and February 28, 2022. Since the values are averaged over $1^\circ\times1^\circ$ area (Smith et al. (1997)), integrations can be performed at each area and summed for total 180×360 sections. Considering the ortho-normality of the spherical harmonics, the squared error of the OLR can be rewritten as follows.

$$\begin{aligned}\mathrm{MSE}_{\epsilon,k}&=\tfrac{1}{4\pi}\sum_{i=0}^{179}\sum_{j=0}^{359}\int_{S_{ij}}\left(\epsilon_{ijk}-\sum_{l=0}^{L}\sum_{m=-l}^{l}e_{lm}Y_{l,m}\right)^2 dS\\ &=\tfrac{1}{4\pi}\left\{\sum_{i=0}^{179}\sum_{j=0}^{359}\epsilon_{ijk}^2\int_{S_{ij}}dS+\sum_{l=0}^{L}\sum_{m=-l}^{l}e_{lm}^2\right.\\ &\left.-2\sum_{l=0}^{L}\sum_{m=-l}^{l}e_{lm}\left(\sum_{i=0}^{179}\sum_{j=0}^{359}\epsilon_{ijk}\int_{S_{ij}}Y_{l,m}dS\right)\right\},\end{aligned} \quad (12)$$

where i,j, and k represent the index of the colatitude, longitude, and time stamp, respectively. S_{ij} is the latitude-longitude gridded area on the Earth surface. The spherical harmonics coefficients should be determined to minimize the squared error. In order words, the partial derivative of the squared error with respect to the spherical harmonics coefficients should be zero.

$$\frac{\partial \mathrm{MSE}_{\epsilon,k}}{\partial e_{lmk}} = -\frac{1}{2\pi}\left(e_{lmk} - \sum_{i=0}^{179}\sum_{j=0}^{359}\epsilon_{ijk}\int_{S_{ij}} Y_{l,m}dS\right). \tag{13}$$

Therefore, the spherical harmonics coefficients can be determined by Eq. (14), and the integral can be calculated using Eq. (6).

$$e_{lmk} = \sum_{i=0}^{179}\sum_{j=0}^{359}\epsilon_{ijk}\int_{S_{ij}} Y_{l,m}dS. \tag{14}$$

If the data product contains missing data region, the calculation of the squared error should be performed with additional care. The albedo coefficient data has some missing data around the polar regions in summer and winter, because of the polar night period. Therefore, there is no measurement data available and also there is no albedo flux towards a spacecraft. In principle, the area with missing data should be excluded from the error calculation. However, because of the ortho-normality of the spherical harmonics, it is more convenient to perform evaluation of the entire sphere. For this reason, we fill the missing data with a dummy value. In the following discussion, the dummy albedo coefficient is shown as α^*_{ijk}, which exists only where valid α_{ijk} is not available.

$$\begin{aligned}\mathrm{MSE}_{\alpha,k} = \frac{1}{4\pi}\Bigg\{&\sum_{i,j}\alpha^2_{ijk}\int_{S_{ij}}dS + \sum_{i,j}\alpha^{*2}_{ijk}\int_{S_{ij}}dS + \sum_{l,m}a^2_{lmk}\\ &-2\sum_{l,m}a_{lmk}\left(\sum_{i,j}\alpha_{ijk}\int_{S_{ij}}Y_{l,m}dS + \sum_{i,j}\alpha^*_{ijk}\int_{S_{ij}}Y_{l,m}dS\right)\Bigg\}.\end{aligned} \tag{15}$$

In order to minimize the error, the partial derivative of the squared error with regard to the dummy data should be zero.

$$\frac{\partial \mathrm{MSE}_{\alpha,k}}{\partial \alpha^*_{ijk}} = \alpha^*_{ijk}\int_{S_{ij}}dS - \sum_{l,m}a_{lmk}\int_{S_{ij}}Y_{l,m}dS. \tag{16}$$

Thus, the dummy data should satisfy Eq. (17). This equation suggests that the dummy data distributes according to the shape of each spherical harmonic and the its weight is equal to the best fit coefficient.

$$\alpha^*_{ijk} = \sum_{l,m}a_{lm}\frac{\int_{S_{ij}}Y_{l,m}dS}{\int_{S_{ij}}dS}. \tag{17}$$

The partial derivative with respect to the spherical harmonics coefficient is described as follows.

$$\begin{aligned}\frac{\partial \mathrm{MSE}_{\alpha,k}}{\partial a_{lmk}} = -\frac{1}{2\pi}\Bigg(&a_{lmk} - \sum_{i,j}\alpha_{ijk}\int_{S_{ij}}Y_{l,m}dS\\ &-\sum_{i,j}\alpha^*_{lmk}\int_{S_{ij}}Y_{l,m}dS\Bigg).\end{aligned} \tag{18}$$

The conditions, where Eq. (16) and Eq. (18) become zero, can be rewritten in the matrix equation as shown in Eq. (19). By solving this equation, the spherical harmonics coefficients for a specific date can be determined.

$$\begin{bmatrix} 1-\sum_{i,j}\frac{\left(\int_{S_{ij}}Y_{0,0}dS\right)^2}{\int_{S_{ij}}dS} & -\sum_{i,j}\frac{\left(\int_{S_{ij}}Y_{1,-1}dS\right)\left(\int_{S_{ij}}Y_{0,0}dS\right)}{\int_{S_{ij}}dS} & \cdots & -\sum_{i,j}\frac{\left(\int_{S_{ij}}Y_{l,l}dS\right)\left(\int_{S_{ij}}Y_{0,0}dS\right)}{\int_{S_{ij}}dS} \\ -\sum_{i,j}\frac{\left(\int_{S_{ij}}Y_{0,0}dS\right)\left(\int_{S_{ij}}Y_{1,-1}dS\right)}{\int_{S_{ijdS}}dS} & 1-\sum_{i,j}\frac{\left(\int_{S_{ij}}Y_{1,-1}dS\right)^2}{\int_{S_{ij}}dS} & \cdots & -\sum_{i,j}\frac{\left(\int_{S_{ij}}Y_{l,l}dS\right)\left(\int_{S_{ij}}Y_{1,-1}dS\right)}{\int_{S_{ij}}dS} \\ \vdots & \vdots & & \vdots \\ -\sum_{i,j}\frac{\left(\int_{S_{ij}}Y_{0,0}dS\right)\left(\int_{S_{ij}}Y_{l,l}dS\right)}{\int_{S_{ijdS}}dS} & -\sum_{i,j}\frac{\left(\int_{S_{ij}}Y_{1,-1}dS\right)\left(\int_{S_{ij}}Y_{l,l}dS\right)}{\int_{S_{ij}}dS} & \cdots & 1-\sum_{i,j}\frac{\left(\int_{S_{ij}}Y_{l,l}dS\right)^2}{\int_{S_{ij}}dS} \end{bmatrix} \begin{bmatrix} a_{0,0,k} \\ a_{1,-1,k} \\ \vdots \\ a_{l,l,k} \end{bmatrix} = \begin{bmatrix} \sum_{i,j}\alpha_{ijk}\int_{S_{ij}}Y_{0,0}dS \\ \sum_{i,j}\alpha_{ijk}\int_{S_{ij}}Y_{1,-1}dS \\ \vdots \\ \sum_{i,j}\alpha_{ijk}\int_{S_{ij}}Y_{l,l}dS \end{bmatrix}. \tag{19}$$

2.4. Seasonal variation

In the previous section, the spherical harmonics coefficients are calculated for each time stamp. Since the OLR and albedo coefficient have seasonal variation, the spherical harmonics coefficients vary over time as well. In order to incorporate the periodic behavior and perform comparison, one time-invariant form and two time-variant forms are considered. The assumed OLR models are described in Eqs. (20)–(22). DOY_k is the corresponding day of year for the time index k.

$$e_{lmk} \simeq e_{lm,0}, \tag{20}$$

$$e_{lmk} \simeq e_{lm,1} + e_{lm,2}\cos\omega t_k + e_{lm,3}\sin\omega t_k, \tag{21}$$

$$\begin{aligned}e_{lmk} \simeq\ & e_{lm,4} + e_{lm,5}\cos\omega t_k + e_{lm,6}\sin\omega t_k\\ &+e_{lm,7}\cos 2\omega t_k + e_{lm,8}\sin 2\omega t_k,\end{aligned} \tag{22}$$

$$\text{where } \omega = \frac{2\pi}{365},\ t_k = \mathrm{DOY}_k - 1. \tag{23}$$

These expressions are analogous to the common models of extraterrestrial solar irradiance presented by Eqs. (24)–(26) from various literatures such as Duffie et al. (2020, 2004, 1983) and Spencer (1971). The model represents the effect of the Earth's eccentric orbit around the Sun, and the variation of extraterrestrial solar irradiance has an influence on the Earth surface temperatures and properties.

$$G_{\mathrm{on}} = G_{\mathrm{sc}}\left(1 + 0.033\cos\frac{360\mathrm{DOY}}{365}\right), \tag{24}$$

$$G_{\mathrm{on}} = G_{\mathrm{sc}}(1.000110 + 0.034221\cos B + 0.001280\sin B + 0.00719\cos 2B + 0.000077\sin 2B), \tag{25}$$

$$\text{where } B = (\mathrm{DOY} - 1)\frac{360}{365}. \tag{26}$$

Besides the effects of the Earth orbit eccentricity, the solar irradiance itself is time-variant, and the corresponding value is called total solar irradiance (TSI). The variation of TSI is related to the 27-day solar rotation period and the 11-year solar activity cycle. However, TSI statistics evaluated by Gueymard (2018) shows that this variation ranges between 1357.10 W/m^2 and 1363.33 W/m^2, which is approximately one order smaller compared to the variation of extraterrestrial solar irradiance caused by the Earth orbit eccentricity. Therefore, in this study, the solar constant G_{sc} is considered to be the long-term average of TSI, and used as the constant parameter.

Now, we define the mean squared error for the OLR and albedo coefficient over time.

$$\mathrm{MSE}_{\epsilon} = \frac{1}{N}\sum_{k=1}^{N}\mathrm{MSE}_{\epsilon,k}, \tag{27}$$

$$\mathrm{MSE}_{\alpha} = \frac{1}{N}\sum_{k=1}^{N}\mathrm{MSE}_{\alpha,k}, \tag{28}$$

where N, in this case, is the number of daily data between March 1, 2000 and February 28, 2022. The model parameters should be determined to minimize the mean squared error. For the time-invariant model shown in Eq. (20), the partial derivative of the mean squared error with regard to the model parameter is described by

$$\frac{\partial \mathrm{MSE}_{\epsilon}}{\partial e_{lm,0}} = -\frac{2}{N}\sum_{l,m}\sum_{k}\left(\left(\sum_{i,j} e_{ijk}\int_{S_{ij}} Y_{l,m}dS\right) - e_{lm,0}\right). \tag{29}$$

Considering Eq. (14), the model parameter $e_{lm,0}$ is determined by the following equation.

$$\sum_{k=1}^{N}(e_{lmk} - e_{lm,0}) = 0. \tag{30}$$

For the time-variant model of Eq. (21), the corresponding condition is described by the following three equations.

$$\sum_{k}(e_{lmk} - (e_{lm,0} + e_{lm,1}\cos\omega t_k + e_{lm,2}\sin\omega t_k)) = 0, \tag{31}$$

$$\sum_{k}\cos\omega t_k(e_{lmk} - (e_{lm,0} + e_{lm,1}\cos\omega t_k + e_{lm,2}\sin\omega t_k)) = 0, \tag{32}$$

$$\sum_{k}\sin\omega t_k(e_{lmk} - (e_{lm,0} + e_{lm,1}\cos\omega t_k + e_{lm,2}\sin\omega t_k)) = 0. \tag{33}$$

These relations can be described in the matrix form Eqs. (34)–(36). By solving this equation, the parameters $e_{lm,0}, e_{lm,1}$, and $e_{lm,2}$ can be determined. It should be noted that this procedure is equivalent to the least square fitting of the model Eq. (21) to the daily parameter e_{lmk}.

$$\boldsymbol{y}_{(21)} = M_{(21)}\boldsymbol{e}_{(21)}, \tag{34}$$

where

$$\boldsymbol{y}_{(21)} = \begin{bmatrix}\sum_k e_{lmk}\\ \sum_k e_{lmk}\cos\omega t_k\\ \sum_k e_{lmk}\sin\omega t_k\end{bmatrix},\ \boldsymbol{e}_{(21)} = \begin{bmatrix}e_{lm,0}\\ e_{lm,1}\\ e_{lm,2}\end{bmatrix}, \tag{35}$$

$$M_{(21)} = \begin{bmatrix}\sum_k 1 & \sum_k\cos\omega t_k & \sum_k\sin\omega t_k\\ \sum_k\cos\omega t_k & \sum_k\cos\omega t_k\cos\omega t_k & \sum_k\cos\omega t_k\sin\omega t_k\\ \sum_k\sin\omega t_k & \sum_k\sin\omega t_k\cos\omega t_k & \sum_k\sin\omega t_k\sin\omega t_k\end{bmatrix}. \tag{36}$$

Similarly, the parameters for the time-variant model in Eq. (22) can be determined by solving the following equation.

$$\boldsymbol{y}_{(22)} = M_{(22)}\boldsymbol{e}_{(22)}, \tag{37}$$

where

$$\boldsymbol{y}_{(22)} = \begin{bmatrix}\sum_k e_{lmk}\\ \sum_k e_{lmk}\cos\omega x_i\\ \sum_k e_{lmk}\sin\omega x_i\\ \sum_k e_{lmk}\cos 2\omega x_i\\ \sum_k e_{lmk}\sin 2\omega x_i\end{bmatrix},\ \boldsymbol{e}_{(22)} = \begin{bmatrix}e_{lm,0}\\ e_{lm,1}\\ e_{lm,2}\\ e_{lm,3}\\ e_{lm,4}\end{bmatrix}, \tag{38}$$

$$M_{(22)} = \begin{bmatrix} \sum_k 1 & \sum_k \cos\omega t_k & \sum_k \sin\omega t_k & \sum_k \cos 2\omega t_k & \sum_k \sin 2\omega t_k \\ \sum_k \cos\omega t_k & \sum_k \cos\omega t_k \cos\omega t_k & \sum_k \cos\omega t_k \sin\omega t_k & \sum_k \cos\omega t_k \cos 2\omega t_k & \sum_k \cos\omega t_k \sin 2\omega t_k \\ \sum_k \sin\omega t_k & \sum_k \sin\omega t_k \cos\omega t_k & \sum_k \sin\omega t_k \sin\omega t_k & \sum_k \sin\omega t_k \cos 2\omega t_k & \sum_k \sin\omega t_k \sin 2\omega t_k \\ \sum_k \cos 2\omega t_k & \sum_k \cos 2\omega t_k \cos\omega t_k & \sum_k \cos 2\omega t_k \sin\omega t_k & \sum_k \cos 2\omega t_k \cos 2\omega t_k & \sum_k \cos 2\omega t_k \sin 2\omega t_k \\ \sum_k \sin 2\omega t_k & \sum_k \sin 2\omega t_k \cos\omega t_k & \sum_k \sin 2\omega t_k \sin\omega t_k & \sum_k \sin 2\omega t_k \cos 2\omega t_k & \sum_k \sin 2\omega t_k \sin 2\omega t_k \end{bmatrix}. \tag{39}$$

Seasonal variation of the albedo coefficient is modeled in the same way.

$$a_{lmk} \simeq a_{lm,0}, \tag{40}$$

$$a_{lmk} \simeq a_{lm,1} + a_{lm,2}\cos\omega t_k + a_{lm,3}\sin\omega t_k, \tag{41}$$

$$a_{lmk} \simeq a_{lm,4} + a_{lm,5}\cos\omega t_k + a_{lm,6}\sin\omega t_k + a_{lm,7}\cos 2\omega t_k + a_{lm,8}\sin 2\omega t_k, \tag{42}$$

where

$$\omega = \frac{2\pi}{365}, \quad t_k = \mathrm{DOY}_k - 1. \tag{43}$$

By evaluating the partial derivative of the mean squared error with respect to the model parameters, the model parameters can be determined. The intermediate formulas are more complex than those of the OLR model, because of the missing data in the albedo data product. However, the parameters of Eqs. (40)–(42) can be calculated with the least square fitting to the daily albedo coefficient, in the same way as the OLR model.

3. Performance evaluation of the OLR and albedo coefficient model

3.1. Representation capability

In this section, we evaluate the representation capability of the proposed model by calculating the root mean square error (RMSE) between the model output and the CERES data product.

$$\mathrm{RMSE}_\epsilon = \sqrt{\mathrm{MSE}_\epsilon}, \tag{44}$$

$$\mathrm{RMSE}_\alpha = \sqrt{\mathrm{MSE}_\alpha}. \tag{45}$$

In order to assess the reasonable complexity of the model, we compare RMSE with respect to the following aspects:

- Spherical harmonics or zonal harmonics
- Maximum degree of spherical/zonal harmonics
- Model complexity for the temporal variation
  - daily: coefficients calculated as shown in 2.3
  - constant: model shown in Eq. (20) and Eq. (40)
  - 1st-order: model shown in Eq. (21) and Eq. (41)
  - 2nd-order: model shown in Eq. (22) and Eq. (42)

Zonal harmonics are the special cases of spherical harmonics, where the order m is zero and the function is axisymmetric around the z-axis.

The evaluation results are shown in Fig. 4 for the OLR and Fig. 5 for the albedo coefficient. In general, the spherical harmonics model has better representation capability than the zonal harmonics model at the same degree. However, the spherical harmonics contain $(n+1)^2$ terms, while the zonal harmonics contain $n+1$ terms, where n is the maximum degree of the spherical or zonal harmonics. Considering this fact, the zonal harmonics model can efficiently represent the OLR and albedo coefficient distributions with less number of parameters.

Significant improvements in both OLR and albedo coefficients are observed when increasing the maximum degree from 1 to 2. This is because OLR and albedo coefficient have roughly symmetrical distribution with respect to the equator. For the OLR zonal harmonics model, minor improvements are achieved by increasing the maximum degree of harmonics up to 8, and then the improvements become marginal. Similarly, for the albedo zonal harmonics model, the minor improvements are observed by increasing the maximum degree of harmonics up to 4, and after that the improvements are marginal.

With respect to the time dependency, the time-invariant model (constant) exhibits larger error than the other models. On the other hand, the difference between the

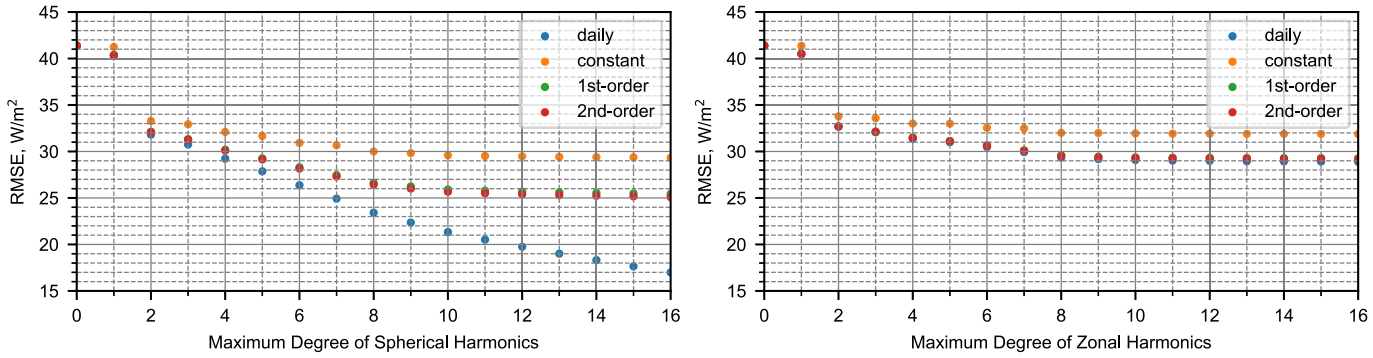

Fig. 4. Time-variant model order and spherical/zonal harmonics degree sensitivity for the OLR distribution.

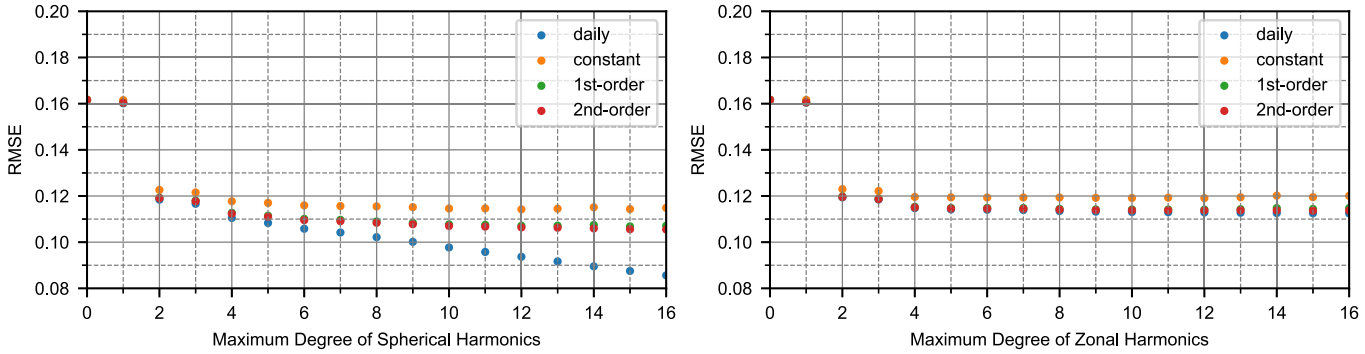

Fig. 5. Time-variant model order and spherical/zonal harmonics degree sensitivity for the albedo coefficient distribution.

time-variant models (1st-order and 2nd-order) is minimal. Also, the zonal harmonics models with the daily parameters present minor improvement compared to the time-variant models (1st-order and 2nd-order). Regarding the spherical harmonics model, the difference between the time-variant model and the daily parameter model increases as the maximum degree of the harmonics increases. This suggests that temporal characteristics of the higher order spherical harmonics cannot be well represented by simple trigonometric functions. One open aspect in this model development and evaluation is the consideration of temporal variation in shorter time scales. For instance, OLR presents a diurnal variation with different amplitudes depending on the land cover type. According to Smith and Rutan (2003), the first principal component of diurnal variation shows the peak value of about $+20\mathrm{W/m^2}$ for land and $+5\mathrm{W/m^2}$ for ocean, relative to the daily average. Since it is difficult to include such short-term variations in the current model, the effect should be considered as an additional uncertainty of the proposed model.

In addition to the accuracy perspective, the zonal harmonics model, which is only latitude dependent, has significant advantages for the spacecraft thermal analysis. Firstly, the zonal harmonics model can be easily applied to different analysis cases. If the model is constructed also longitude dependent, detailed spacecraft orbit information has to be specified for each analysis case, including the exact time or the local longitude. Such detailed information is typically not available during the early design phases, and so it costs additional effort to setup reasonable assumptions. Secondly, LEO satellites fly over the entire longitudinal range. That means that the satellite thermal design should withstand the thermal conditions of arbitrary longitude. Therefore, it is important that the models represent the critical conditions within the entire longitudinal range, but the capability to represent various environments as a function of longitude is not essential.

3.2. Heat flux in the orbit

Since the developed models are intended for evaluating the thermal environment of the spacecraft, the ultimate interest is the accuracy of the heat flux received in the orbit. In this section, we evaluate the received heat flux in the orbit and compare the outcomes when using the constructed model and the CERES data products. For the spacecraft thermal analysis, the infrared emission and albedo reflection from the Earth surface are normally assumed to be Lambertian. However, in reality, these radiations have anisotropic characteristics, depending on the Earth surface type and cloud coverage. These characteristics can be described by the ADMs, but only limited examples can be found, where the ADMs are used to evaluate fluxes in the orbit. Vielberg and Kusche (2020) presented the radiation pressure evaluation method for the LEO satellite, based on the hourly CERES SYN1deg data product with the ADM consideration. Similarly, Hakuba et al. (2024) applied the ADMs based on Suttles et al. (1988) for evaluating the shortwave radiation pressure on different spacecraft geometries. In this study, the flux calculation by using the constructed model is based on the Lambertian assumption for the simplicity of the analysis, and the reference calculation based the CERES data product considers the anisotropic characteristics by using the ADMs, referring to the method presented in Vielberg and Kusche (2020).

3.2.1. Evaluation method

Earth infrared and albedo fluxes received by the satellite are calculated by integrating the local flux from the Earth surface over the satellite's field of view. With the Lambertian assumption, the Earth infrared flux from a differential area to the satellite can be evaluated as the product of the local OLR $\epsilon(\theta,\varphi)$, and the view factor. Additionally, including the anisotropic factor R_{ADM}, the total flux is calculated by Eq. (46), with the related geometrical parameters are shown in Fig. 6.

$$q_{\mathrm{infrared}} = \iint \frac{R_{\mathrm{ADM}}\epsilon(\theta,\varphi)\cos\Theta_0\cos\Theta_1}{\pi S^2} R^2 \sin\theta d\varphi d\theta. \tag{46}$$

The albedo flux from a differential area is calculated in a similar way, but the local flux intensity corresponds to the product of the albedo coefficient $\alpha(\theta,\varphi)$, extraterrestrial solar irradiance G_{on}, and the cosine of the solar zenith

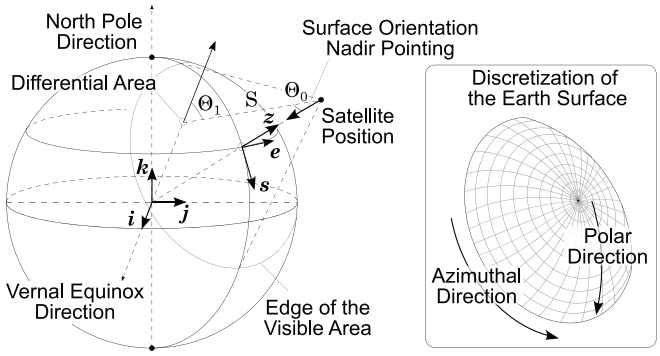

Fig. 6. Flux integration on the Earth surface.

angle Φ. Thus, the total flux is calculated by Eq. (47). It should be noted that, for the area which is not illuminated by the Sun ($\Phi \leqslant 0$), the local albedo flux becomes zero.

$$q_{\text{albedo}} = \iint \frac{R_{\text{ADM}} G_{\text{on}} \alpha(\theta,\varphi) \cos\Theta_0 \cos\Theta_1 \cos\Phi}{\pi S^2} R^2 \times \sin\theta d\varphi d\theta. \tag{47}$$

The anisotropic factor R_{ADM} is specified by the ADMs. Although the latest ADMs, which are applied to the CERES data processing, are presented in Su et al. (2015a,b), we use the ERBE (Earth Radiation Budget Experiment) ADMs presented in Suttles et al. (1988, 1989) for its simplicity, following the method presented in Vielberg and Kusche (2020). In this model, five land cover types and cloud coverage are used to specify the scene type, and then the anisotropic factor is selected based on the angular relationship between the Sun, the satellite, and the Earth surface normal. Regarding the land cover type, the dataset MODIS/Terra + Aqua Land Cover Type Yearly L3 Global 0.05Deg CMG V061 (Friedl and Sulla-Menashe (2022)) is utilized. In this dataset, 17 land cover types are specified for each $0.05^\circ \times 0.05^\circ$ grid area. We mapped these types into four land cover types for each $1^\circ \times 1^\circ$ grid area as shown in Fig. 7, and the resulting simplified land cover map is presented in Fig. 8. Regarding the cloud overage, the required data is provided within the CERES SYN1deg data product at the same temporal and spatial resolution as those of OLR and albedo coefficient. Based on this data product, the cloud coverage is classified to clear sky (0–5% coverage), partly cloudy (5–50% coverage), mostly cloudy (50–95% coverage), and overcast (95–100% coverage) for specifying the scene type.

In this study, calculations of Eqs. (46) and (47) are performed numerically, with the three preparation steps related to different coordinate systems. First, the satellite position and Sun orientation are specified in geocentric equatorial (IJK) coordinate system. The satellite orbit is assumed to be a Keplerian orbit around the Earth, and the satellite position can be calculated from the orbital elements, based on the basic astrodynamics relations presented in Vallado and McClain (2013). The Sun orientation in the IJK coordinate system can be described by the right ascension α_{sun}, and the declination of the Sun δ_{sun}, as shown in Eq. (48). These parameters are estimated by using the method presented in Michalsky (1988) and Zhang et al. (2021).

$$\begin{bmatrix} \cos\alpha_{\text{sun}} \cos\delta_{\text{sun}} \\ \sin\alpha_{\text{sun}} \cos\delta_{\text{sun}} \\ \sin\delta_{\text{sun}} \end{bmatrix}. \tag{48}$$

Second, the horizontal (SEZ) coordinate system is defined, and the Earth surface is discretized for numerical integration. The orientation of the SEZ coordinate system is defined by three axes: the first axis pointing to south, the second axis pointing to east, and the third axis pointing to zenith towards the satellite, as shown in Fig. 6. Commonly, the origin of the SEZ coordinate system is located at the observer on the Earth surface, but we shift the origin to the Earth center in this discussion for convenience of the discretization. Assuming the satellite position is described by polar parameters $(r_{\text{sat}}, \theta_{\text{sat}}, \varphi_{\text{sat}})$ in the IJK coordinate system, the rotation between the IJK and SEZ coordinate systems is described by

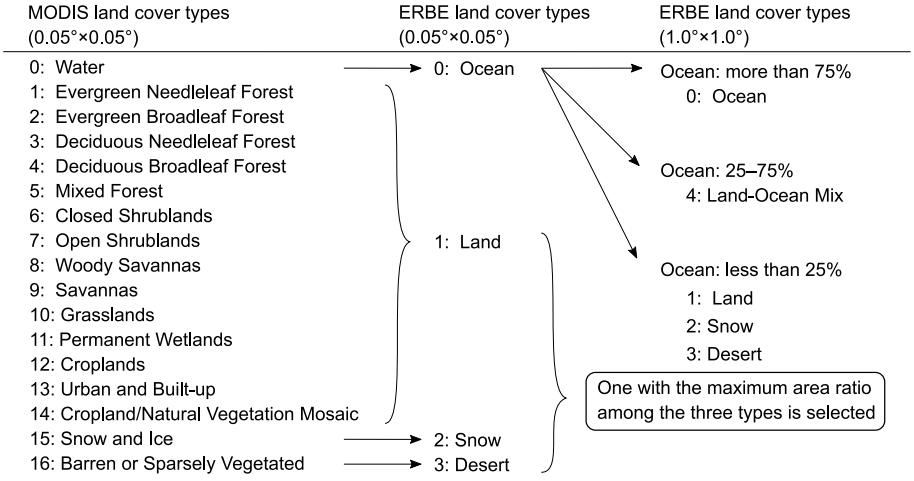

Fig. 7. Mapping assumption from MODIS land cover types to ERBE land cover types.

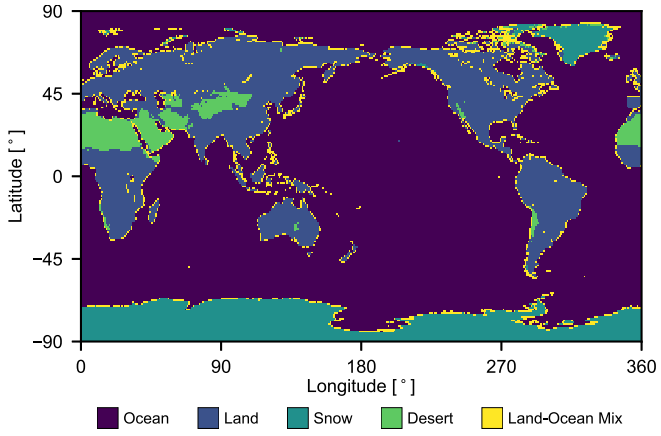

Fig. 8. Simplified land cover map to determine the scene type for ADM.

$$\begin{bmatrix} x_{ijk} \\ y_{ijk} \\ z_{ijk} \end{bmatrix} = \begin{bmatrix} \cos\theta_{sat}\cos\varphi_{sat} & -\sin\varphi_{sat} & \sin\theta_{sat}\cos\varphi_{sat} \\ \cos\theta_{sat}\sin\varphi_{sat} & \cos\varphi_{sat} & \sin\theta_{sat}\sin\varphi_{sat} \\ -\sin\theta_{sat} & 0 & \cos\theta_{sat} \end{bmatrix} \begin{bmatrix} x_{sez} \\ y_{sez} \\ z_{sez} \end{bmatrix}. \tag{49}$$

For the actual calculation, the Earth surface within the satellite's field of view is discretized to 180×720 sections in polar and azimuthal directions, as illustrated in Fig. 6. Third, the local OLR and albedo coefficient at each discretized area is specified in the Earth-centered Earth-fixed (ECEF) coordinate system. The ECEF coordinate system is acquired by rotating the IJK coordinate system around the Earth axis.

$$\begin{bmatrix} x_{ijk} \\ y_{ijk} \\ z_{ijk} \end{bmatrix} = \begin{bmatrix} \cos\lambda & -\sin\lambda & 0 \\ \sin\lambda & \cos\lambda & 0 \\ 0 & 0 & 1 \end{bmatrix} \begin{bmatrix} x_{ecef} \\ y_{ecef} \\ z_{ecef} \end{bmatrix}. \tag{50}$$

During the orbit flux evaluation, the rotation angle λ is specified from the initial value λ_0, which is given as part of the test case parameters, and the elapsed time Δt divided by the sidereal day $T_{sidereal}$.

$$\lambda = \lambda_0 + \frac{2\pi\Delta t}{T_{sidereal}}. \tag{51}$$

Using Eqs. (49) and (50), the positions and orientations can be transformed between different coordinate systems. Finally, the integrands in Eqs. (46) and (47) are calculated for each discretized area and summed for the entire area visible from the satellite. The OLR and albedo coefficient values at each discretized area are based on those at the center of each area.

3.2.2. Test case selection

For the model evaluation, test orbit parameters are selected, considering typical low Earth orbit satellites. According to the statistical study by Sanad et al. (2020), the majority of remote sensing satellites use circular sun-synchronous orbits, as well as other orbits such as International Space Station (ISS) orbits and some mid-inclination orbits. Other recent studies by del Portillo et al. (2019, 2021) and Chougrani et al. (2024) summarize the technical information of the large constellations for satellite internet services, such as Telesat, OneWeb, Starlink and Kuiper. With regard to the orbit configuration, typically such constellation system utilizes a combination of polar orbits and inclined orbits. This configuration enables the global coverage and better communication capacity for the populated regions. For the inclined orbit, the inclination around 50° is often used, but smaller inclinations, such as 33° and 42° for Kuiper, are also utilized. Considering these trends, three sets of altitude and inclination values are selected as shown in Table 1, which corresponds to SSO, ISS orbit and mid-inclination orbit, respectively. Theoretically, the exact date and time for each analysis point should be specified, in order to precisely determine the physical conditions. However, for simplicity and evaluation consistency, the OLR and albedo coefficient distributions, the solar orientation, and the solar irradiation are specified based on the date information, and it is assumed that the initial rotation angle, λ_0, can be independently variated. The selected date range for this evaluation is one year from March 1, 2022, which does not overlap with the period used for the model construction. Under this assumption, a RAAN value has minor importance on the Earth infrared flux evaluation, because variation of the initial rotation angle is sufficient to cover the different area of the Earth surface. For the albedo flux, on the other hand, a RAAN value specifies the solar zenith angle. In each evaluation case, a RAAN value is selected to be the same as the right ascension of the Sun, so that the satellite receives intensive albedo flux around the local noon. Regarding the satellite orientation, the analyzed surface is assumed to be fixed in the nadir direction, where the influence of the Earth infrared and albedo fluxes become maximum.

3.2.3. Evaluation result

The infrared and albedo fluxes in the orbits, specified in Table 1, are calculated using the constructed model and the CERES data products. Considering the evaluation results in 3.1, the models used in this section are zonal harmonics with the maximum degree of 8. Regarding the temporal variation, the constant model and the 1st-order time-variant model are evaluated. Figs. 9 and 10 illustrate the RMSE of the flux calculation results between the model and the CERES data products. For both infrared and albedo flux, the notable reductions in RMSE are observed by increasing the maximum degree of the zonal harmonics from 1 to 2. For the higher degrees, the improvements diminish, and especially for the albedo flux, the enhancements become marginal after the maximum degree of 4. These results are consistent with the previous discussion.

Meanwhile different types of orbits exhibit some specific characteristics. Firstly, lower altitude orbits show larger RMSE. At lower altitudes, the OLR and albedo fluxes increase due to the large surface visibility. Secondly, large inclination orbits show significant RMSE reduction by increasing the maximum degree of the zonal harmonics.

Table 1
Orbital parameters for the model evaluation. For each orbit, the received infrared and albedo flux are evaluated for one complete orbit at every 2° interval. The total number of evaluation points is 3 × 2365200.

Altitude	Inclination	Eccentricity	Date (JJJJ-MM-DD)	RAAN	Initial rotation angle, λ_0	Orbit type
650 km	98°	0.0	2022–03-01 – 2023–02-28	α_{sun} of the day	Every 10°	SSO
400 km	51°	0.0	2022–03-01 – 2023–02-28	α_{sun} of the day	Every 10°	ISS
590 km	33°	0.0	2022–03-01 – 2023–02-28	α_{sun} of the day	Every 10°	mid-inclination

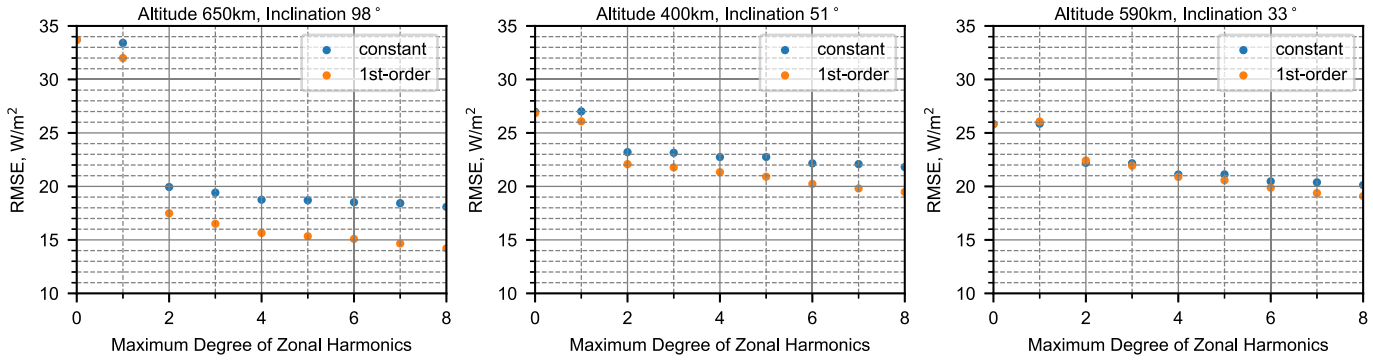

Fig. 9. RMSE of infrared flux in the orbit between the CERES data and the model.

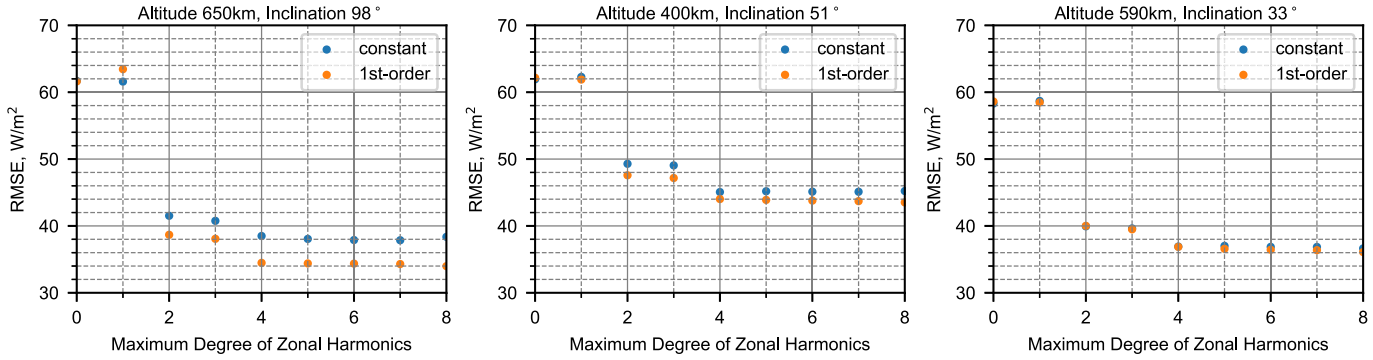

Fig. 10. RMSE of albedo flux in the orbit between the CERES data and the model.

This is attributed to the symmetrical distributions of the OLR and albedo coefficient with respect to the equator, which is better represented by 2nd or higher degree zonal harmonics, and the high inclination orbit is more sensitive to the polar region characteristics. Thirdly, the discrepancy between the constant model and the 1st-order model is larger for high inclination orbits. Regions far from the equator exhibits greater seasonal environmental variation, which also affects the OLR and albedo coefficient distribution. Consequently, high inclination orbits reflect the seasonal variation more significantly than low inclination orbits.

Given the prevalence of SSO in Earth satellite missions, incorporating the time-variant model is essential. Regarding the degree of zonal harmonics, 2nd or higher degree is recommended for the reasonable evaluation of the

Table 2
OLR zonal harmonics model parameters for maximum degree of 4. The corresponding RMSE value is 31.38267 W/m^2. The parameters and RMSE value are presented with seven significant digits.

i	$e_{i,1}$	$e_{i,2}$	$e_{i,3}$
0	846.5127	−11.71082	−5.007011
1	9.35777	−38.16887	−11.64853
2	−84.64440	−4.148072	−1.399822
3	12.61828	−24.18759	−6.167508
4	−22.10449	6.610096	2.565666

Table 3
Albedo coefficient zonal harmonics model parameters for maximum degree of 4. The corresponding RMSE value is 0.1147665. The parameters and RMSE value are presented with seven significant digits.

i	$a_{i,1}$	$a_{i,2}$	$a_{i,3}$
0	1.135866	0.02805531	0.004863929
1	−0.02568558	0.1560044	0.02306313
2	0.4129173	0.03064179	0.01157133
3	−0.04970988	0.03961453	0.02163336
4	0.1107932	0.002905725	−0.01802534

OLR and albedo flux in the orbit. For the simplicity and considering the limited improvement by increasing the degree, the 4th-degree zonal harmonics with 1st-order time-variant model is selected for the further evaluation. The corresponding model parameters and RMSE values are summarized in Table 2 and Table 3.

Figs. 11–13 and Figs. 14–16 present the flux calculation results for the infrared and albedo, respectively. The light blue lines show the flux calculated with the CERES data product, and the red lines show the flux calculated with the 1st-order time-variant maximum 4th-degree zonal harmonics model. Additionally, the green lines present the cal-

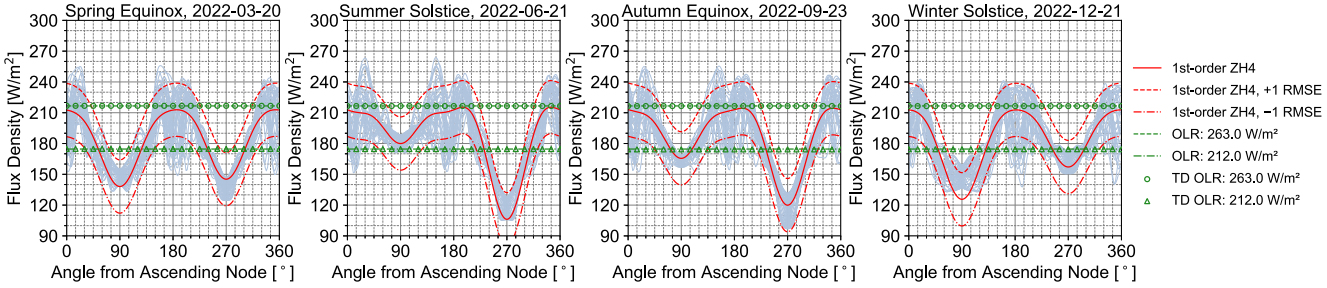

Fig. 11. Infrared flux received by the satellite in 650 km, 98° inclination orbit. 91.2% of the data points calculated with the CERES data are within ±1 RMSE range of the 1st-order time-variant zonal harmonics model with maximum degree of 4.

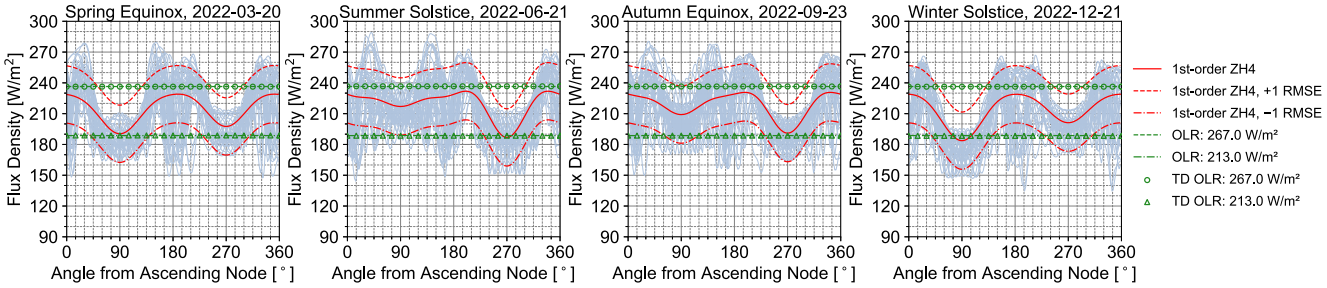

Fig. 12. Infrared flux received by the satellite in 400 km, 51° inclination orbit. 83.2% of the data points calculated with the CERES data are within ±1 RMSE range of the 1st-order time-variant zonal harmonics model with maximum degree of 4 (ZH4).

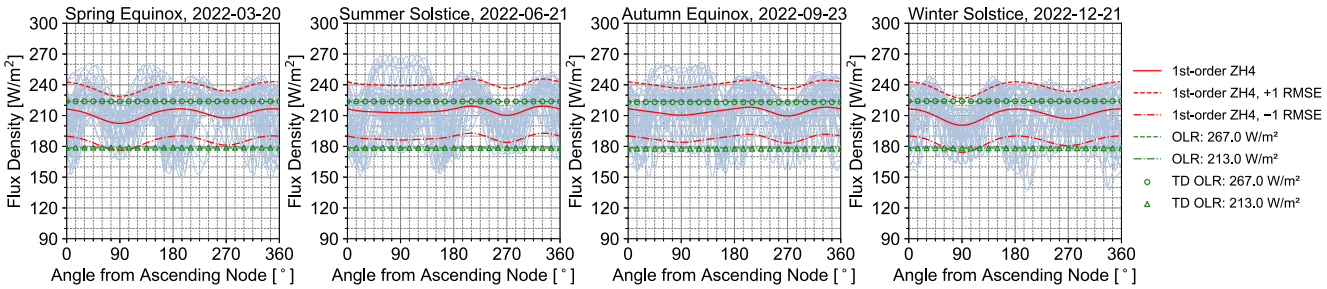

Fig. 13. Infrared flux received by the satellite in 590 km, 33° inclination orbit. 82.0% of the data points calculated with the CERES data are within ±1 RMSE range of the 1st-order time-variant zonal harmonics model with maximum degree of 4 (ZH4).

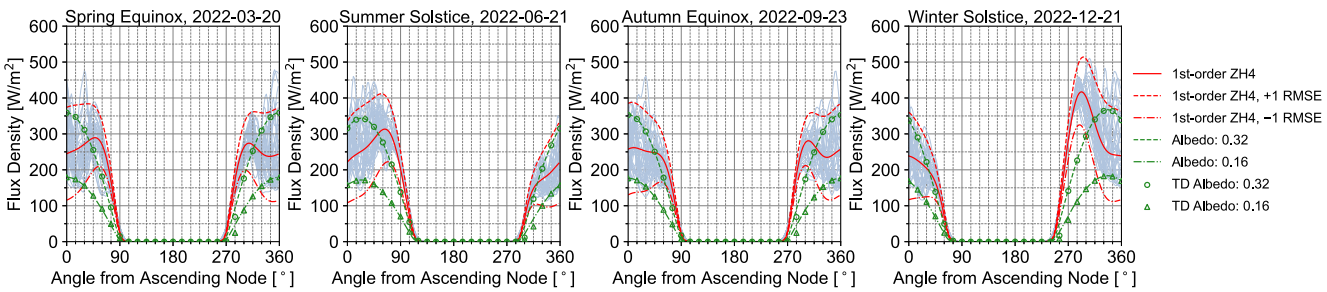

Fig. 14. Albedo flux received by the satellite in 650 km, 98° inclination orbit. 82.0% of the data points calculated with the CERES data are within ±1 RMSE range of the 1st-order time-variant zonal harmonics model with maximum degree of 4 (ZH4).

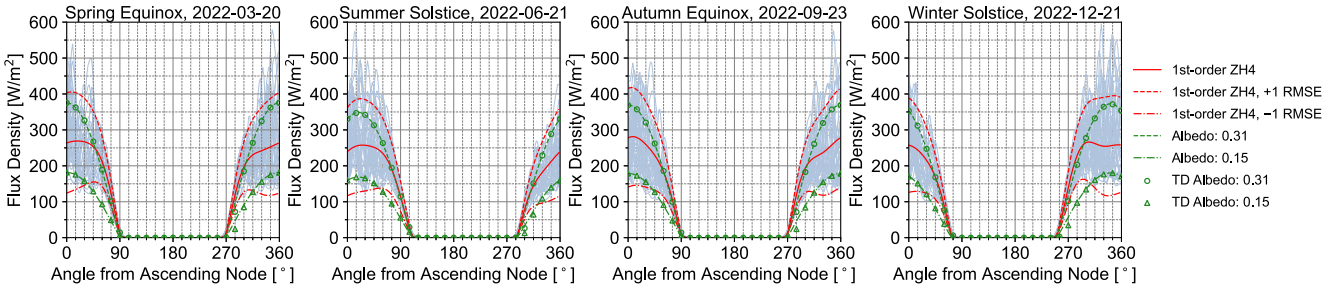

Fig. 15. Albedo flux received by the satellite in 400 km, 51° inclination orbit. 82.9% of the data points calculated with the CERES data are within ±1 RMSE range of the 1st-order time-variant zonal harmonics model with maximum degree of 4 (ZH4).

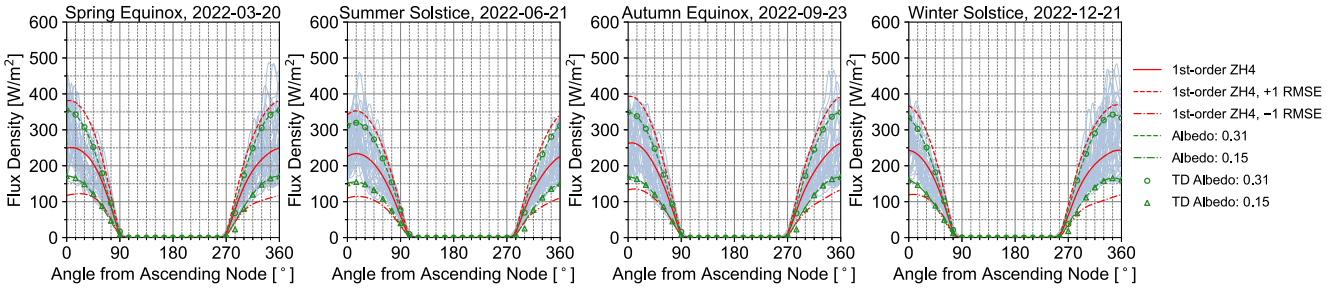

Fig. 16. Albedo flux received by the satellite in 590 km, 33° inclination orbit. 82.9% of the data points calculated with the CERES data are within ±1 RMSE range of the 1st-order time-variant zonal harmonics model with maximum degree of 4 (ZH4).

culated infrared flux based on the uniform OLR or albedo coefficient assumption. This calculation is performed numerically based on the Eq. (46) and Eq. (47) with constant ϵ and α, and by using the thermal analysis software Thermal Desktop® (TD). The uniform values for OLR and albedo coefficient are selected based on Anderson et al. (2001) for hot and cold cases.

For all cases shown in Figs. 11–13, the evaluation starts from the ascending node and ends after one complete orbit. The initial infrared flux is relatively high because of the equator region. Then, the flux decreases as the satellite moves to the high latitude region of the northern hemisphere, and increases again as the satellite moves to the equator region. Afterwards, the infrared flux decreases as the satellite moves to the high latitude region of the southern hemisphere, and increases again as the satellite moves back to the equator region. Although this is the general trend, it is clearly visible that the infrared flux has complex dependency on the orbit type and the time of the year.

The albedo flux analyses, shown in Figs. 14–16, start at the ascending node and the test cases assume that RAAN equals the right ascension of the Sun. Thus, the initial albedo flux is high, and the flux decreases as the satellite flies to the large solar zenith angle area. While the satellite is in the Earth eclipse, there is no albedo flux. After the satellite comes back to the illuminated side, the albedo flux increases again. Since the major driver of the albedo flux is the solar zenith angle, those characteristics are common behavior for all the orbit types and seasons. However, some orbit specific characteristics can be seen as well. For the lower inclination orbits, the general trend of the albedo flux follows the solar zenith angle. On the other hand, the combined effect from the solar zenith angle and the local albedo coefficient causes complex trend over one orbit for the high inclination orbits.

For both infrared and albedo flux, the 4th-degree zonal harmonics model represents the general trend for different orbits and seasons. Conversely, the flux calculation results for the uniform OLR and albedo coefficient present only the simplified flux evolution. The infrared flux is constant over the orbit, and the albedo flux is approximately proportional to the cosine of the solar zenith angle. Thus, the application of the constructed model is useful for incorporating the dynamic variation of the infrared and albedo flux in the orbit. On the other hand, the effect of local OLR and albedo coefficient variation is not negligible, and this uncertainty has to be considered in the thermal analysis. As discussed in the previous section, the error between the models and CERES data products are presented in Figs. 4 and 5. With additional offset corresponding to these RMSE value, hot and cold cases of the OLR and albedo flux can be calculated. The calculated fluxes with ±1 RMSE offset are shown in dashed line and dashdotted line in Figs. 11–16.

As shown in these figures, the majority of the CERES data points, from 82.0% to 91.2%, are covered within the ±1 RMSE range of the model. This suggests that the heat flux in the orbit can exceed the ±1 RMSE range only for a limited period of time during orbiting. Therefore, except for an object, that is directly exposed to the external environment and has specifically low thermal time constant, the analysis with ±1 RMSE offset should be able to cover var-

ious flux conditions caused by the local OLR and albedo coefficient distribution. In the meantime, there are different characteristics in the coverage ratio depending on the types of flux and orbit. Regarding the infrared flux, the evaluation results for SSO cases show higher coverage compared to the other lower inclination orbit results. This characteristic is likely because the OLR widely varies over longitude around the equator region. For the albedo flux, all orbit cases show around 82–83% coverage. The major part of deviations from the model ±1 RMSE range are observed around the terminator region, where the solar zenith angle is around 90° and the significant anisotropic reflection occurs. In this region, the realistic albedo flux is higher than the predication based on the Lambertian assumption. This effect is also mentioned in Anderson et al. (2001), and the additional albedo correction term is recommended for the high solar zenith angle region or an orbit with high solar beta angle. Thus, the coverage for the low solar zenith angle region is well higher than 82–83%. Considering these characteristics, it is suggested that the offset should be carefully selected especially for the low inclination, low altitude orbits, and terminator orbits.

3.3. Demonstration of temperature calculation

The calculated incident heat flux is intended for evaluating the spacecraft temperatures. Since resulting temperature is strongly influenced by the various spacecraft side parameters, such as optical properties, heat capacity, conductive and radiative coupling with other components, it is significantly difficult to establish a generally representative analysis case. In this section, the temperature calculation is demonstrated for a simple case, in order to visualize the variable heat flux effect on spacecraft temperatures.

In this evaluation case, we calculate the temperature of a spacecraft surface oriented in the nadir direction, modeled as a single-node flat plate with unit area, as illustrated in Fig. 17. The emissivity and absorptivity of the surface are set to 0.9, assuming that the surface is sensitive to both the albedo and infrared flux. For the unit-area single-node model, the transient temperature is evaluated by Eq. (52).

$$C_{\mathrm{node}}\frac{dT_{\mathrm{node}}}{dt}=\alpha_s\dot{Q}_{\mathrm{sun}}+\epsilon_s\dot{Q}_{\mathrm{ir}}+\alpha_s\dot{Q}_{\mathrm{al}}-\epsilon_s\sigma\left(T_{\mathrm{node}}^4-T_\infty^4\right). \tag{52}$$

In this equation, the conductive and radiative coupling with other components are neglected, and the rear side of the surface is assumed to be isolated from the surrounding environment. With regard to the heat capacity of the node, two different values: $13440\,\mathrm{J/m^2K}$ and $1344\,\mathrm{J/m^2K}$ are analyzed. These values correspond to the heat capacity of 5.0 mm and 0.5 mm thickness aluminum plate, with a density of $2800\,\mathrm{kg/m^3}$ and a specific heat capacity of $960\,\mathrm{J/kgK}$, based on the 7075 aluminum alloy properties (Davis (1993)).

Figs. 18–23 present the transient temperature results of the single-node model in different orbits and seasons. Same as the flux analysis, the light blue lines represent the calculated temperatures based on the CERES data product, red lines based on the proposed model, and the green lines based on the uniform OLR and albedo coefficient assumption. Additionally, the results with Thermal Desktop® (TD) for the uniform OLR and albedo coefficient cases are included to support the validity of the numerical calculation. The temperature calculations are performed for three orbit rotations, and each plot presents the temperature profile of the last orbit rotation, starting from the ascending node. In general, the temperature varies primarily due to the day-night cycle of the albedo flux, with additional effect by the infrared and solar flux.

The results based on the proposed model closely represent the trend of the CERES based results for different orbit, seasons, and heat capacity cases. For instance, in the high inclination orbit and the low heat capacity cases shown in Fig. 19, the complex temperature variations occur around the shadow to sunlit transition region. These characteristics are difficult to be captured by the uniform assumption, but the results by the proposed model follow the temperature variation characteristics. In contrast, the difference between the proposed model and the uniform

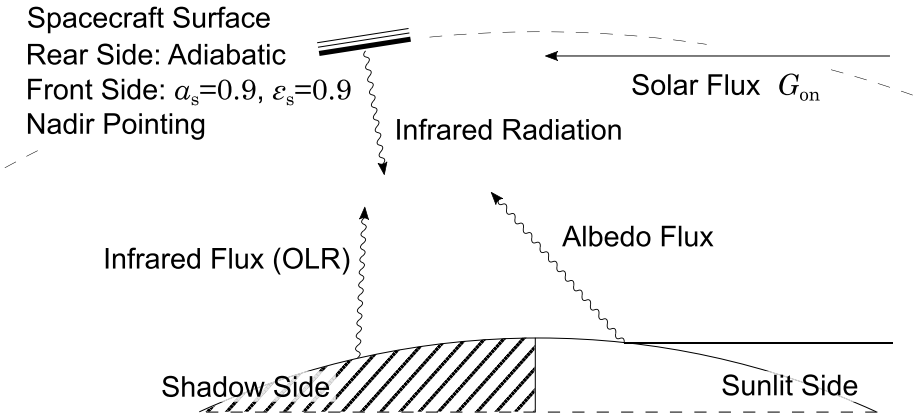

Fig. 17. Temperature Calculation Assumptions for single-node Spacecraft Surface.

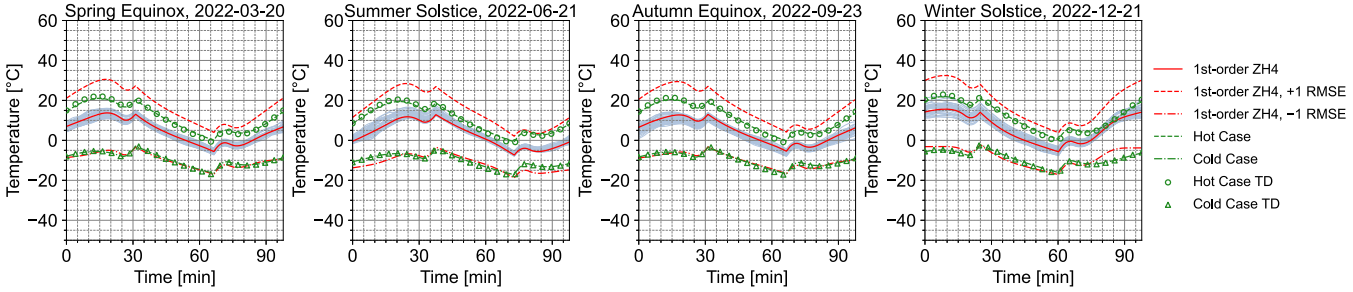

Fig. 18. Transient temperature results of the spacecraft surface with 13440.0 J/m^2 heat capacity in 650 km, 98° inclination orbit.

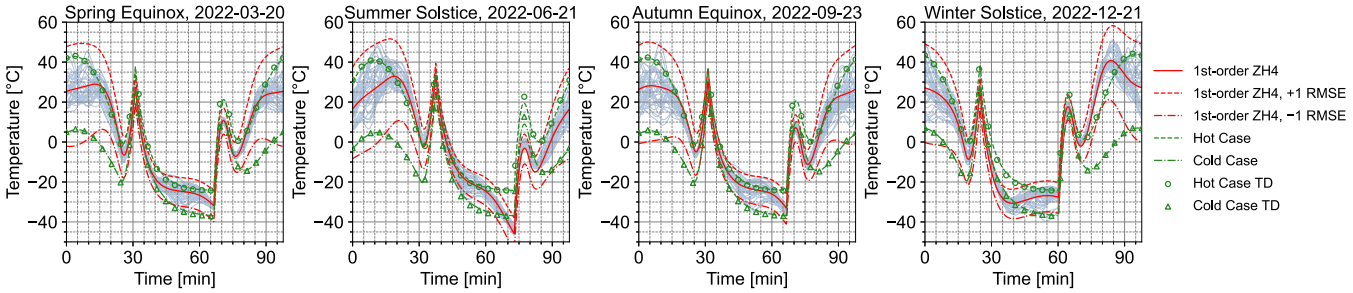

Fig. 19. Transient temperature results of the spacecraft surface with 1344.0 J/m^2 heat capacity in 650 km, 98° inclination orbit.

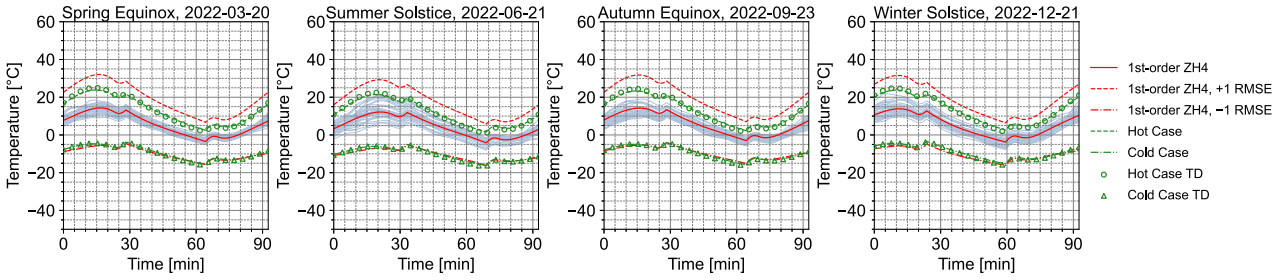

Fig. 20. Transient temperature results of the spacecraft surface with 13440.0 J/m^2 heat capacity in 400 km, 51° inclination orbit.

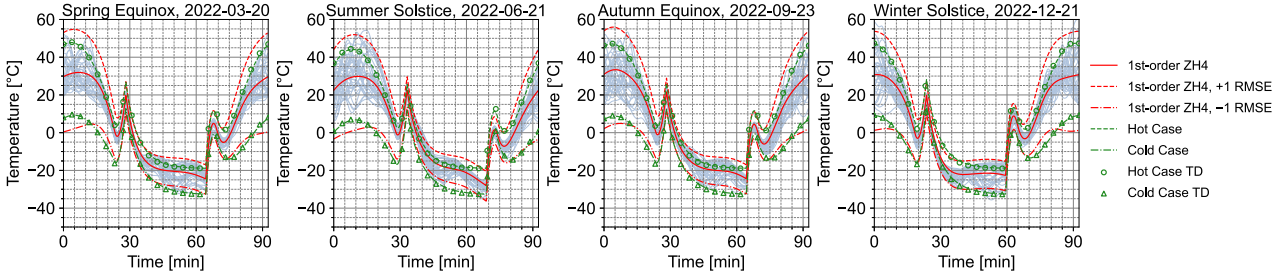

Fig. 21. Transient temperature results of the spacecraft surface with 1344.0 J/m^2 heat capacity in 400 km, 51° inclination orbit.

assumption is relatively minor for the lower inclination cases (Figs. 20–23). This is because the OLR and albedo coefficient variation is less significant within the low latitude region. Also, for the high heat capacity cases (Figs. 18, 20 and 22), the overall behaviors of the proposed model and the uniform assumption are similar because the short period of flux inaccuracy does not significantly affect the resulting temperatures. Consequently, the proposed model is particularly useful for orbits covering various latitude regions and low heat capacity conditions, where the OLR and albedo coefficient variation significantly affects the temperature variation.

With respect to the amount of uncertainties for hot and cold cases, the proposed model with ±1 RMSE offset sufficiently covers the temperature variations of the CERES based results. However, for the high heat capacity results and certain periods in low heat capacity results, the amount of temperature offset exceeds the variations of the CERES

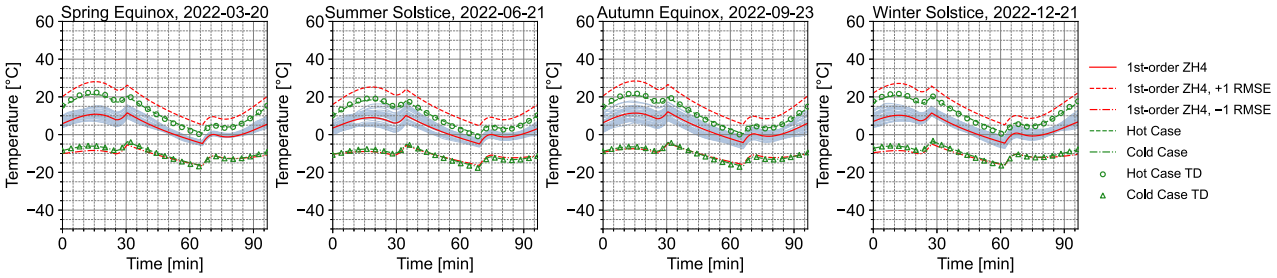

Fig. 22. Transient temperature results of the spacecraft surface with 13440.0 J/m^2 heat capacity in 590 km, 33° inclination orbit.

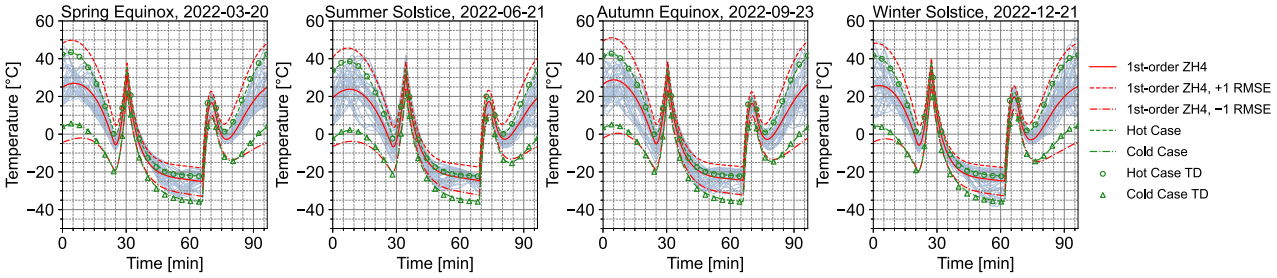

Fig. 23. Transient temperature results of the spacecraft surface with 1344.0 J/m^2 heat capacity in 590 km, 33° inclination orbit.

based results by more than 10 °C. This suggests that the considered uncertainties could potentially be reduced to less than ±1 RMSE, which helps to avoid over-sizing of the thermal control system. Nevertheless, because temperature sensitivity with respect to the incident albedo and infrared flux depends on various spacecraft parameters, the amount of uncertainties must be carefully selected considering the possible spacecraft configurations. Therefore, further studies should be performed to establish the generally applicable and less conservative uncertainty values for the spacecraft thermal analysis.

4. Conclusion

In this study, we proposed the simplified model for describing the OLR and albedo coefficient distributions over the Earth surface, intended for the spacecraft thermal analysis. The model utilizes spherical harmonics and trigonometric functions for representing the spatial distribution and temporal variation, respectively. The model parameters are calculated to minimize the RMSE between the model output and the CERES data product. Generally, spherical harmonics provide a superior description of the OLR and albedo coefficient distributions compared to the zonal harmonics of the same maximum degree. However, considering the number of terms used, zonal harmonics demonstrate better representation capability with fewer terms, because of the distinct latitude dependency of the OLR and albedo coefficient. Furthermore, the simplicity of the zonal harmonics model makes it more suitable for the spacecraft thermal analysis. Regarding the maximum degree of zonal harmonics, while models with higher degree zonal harmonics enhance the description capability, the actual RMSE reduction becomes marginal beyond eighth degree for the OLR, and fourth degree for the albedo coefficient. Consequently, 1st-order time-variant zonal harmonics model with the maximum degree of 4 was employed to evaluate heat flux in various orbits, including SSO, ISS orbit, and mid-inclination orbit. The results indicate that the flux calculated with the model represents the flux variations in various orbital conditions and seasons. By incorporating ±1 RMSE as the model uncertainties, the OLR and albedo coefficient distributions for hot and cold cases can be formulated. The flux calculation results show that majority of the CERES data points, from 82.0% to 91.2%, are covered within the ±1 RMSE range for different orbit types. Additionally, the temperature calculation results indicate that ±1 RMSE range sufficiently covers the temperature variations of the CERES data based results, but the considered uncertainties could be reduced for certain scenarios. Since the temperature sensitivity with respect to the incident heat flux depends on various spacecraft parameters, further studies are recommended to establish the generally applicable and less conservative uncertainty value for the spacecraft thermal analysis.

Declaration of Competing Interest

The authors declare that they have no known competing financial interests or personal relationships that could have appeared to influence the work reported in this paper.

Acknowledgments

The utilized data product CERES SYN1deg-Day Ed4.1 was obtained from the NASA Langley Research Center CERES ordering tool at https://ceres.larc.nasa.gov/data/. The author appreciate the CERES project team for making these valuable data resources available.

References

Anderson, B.J., Justus, C.G., Batts, G.W., 2001. Guidelines for the selection of near-Earth Thermal Environment Parameters for Spacecraft Design. Technical Report NASA/TM-2001-211221. Marshall Space Flight Center.

Atkinson, K., Han, W., 2012. Spherical Harmonics and Approximations on the Unit Sphere: An Introduction. Springer, Berlin, Heidelberg. https://doi.org/10.1007/978-3-642-25983-8.

Borden, M., Lewis, D., Ochoa, H., et al., 2017. Thermal, structural, and optical analysis of a balloon-based imaging system. Publ. Astron. Soc. Pac. 129 (973), 035001. https://doi.org/10.1088/1538-3873/129/973/035001.

Chougrani, H., Kodheli, O., Georganaki, A., et al., 2024. Connecting space missions through NGSO constellations: feasibility study. Front. Commun. Networks 5. https://doi.org/10.3389/frcmn.2024.1356484, URL: https://www.frontiersin.org/articles/10.3389/frcmn.2024.1356484.

Davis, J.R., (Ed.), 1993. ASM Specialty Handbook: Aluminum and Aluminum Alloys. ASM International.

del Portillo, I., Cameron, B.G., Crawley, E.F., 2019. A technical comparison of three low earth orbit satellite constellation systems to provide global broadband. Acta Astronautica, 159, 123–135. URL: https://www.sciencedirect.com/science/article/pii/S0094576518320368. doi:10.1016/j.actaastro.2019.03.040.

DiDonato, A.R., 1982. Recurrence relations for the indefinite integrals of the associated legendre functions. Math. Comput. 38 (158), 547–551, URL: http://www.jstor.org/stable/2007289.

Doelling, D.R., Loeb, N.G., Keyes, D.F. et al., 2013. Geostationary Enhanced Temporal Interpolation for CERES Flux Products. J. Atmos. Ocean. Technol., 30(6), 1072–1090. URL: https://journals.ametsoc.org/view/journals/atot/30/6/jtech-d-12-00136_1.xml. doi:10.1175/JTECH-D-12-00136.1.

Doelling, D.R., Sun, M., Nguyen, L.T. et al., 2016. Advances in Geostationary-Derived Longwave Fluxes for the CERES Synoptic (SYN1deg) Product. J. Atmos. Ocean. Technol., 33(3), 503–521. URL: https://journals.ametsoc.org/view/journals/atot/33/3/jtech-d-15-0147_1.xml. doi:10.1175/JTECH-D-15-0147.1.

Duffie, J.A., Beckman, W.A., Blair, N., 2020. Solar Engineering of Thermal Processes, Photovoltaics and Wind. John Wiley & Sons, Ltd.. https://doi.org/10.1002/9781119540328.ch1.

ECSS-E-ST-10-04C, 2008. ECSS-E-ST-10-04C – Space environment.

Friedl, M., Sulla-Menashe, D., 2022. Modis/terra+aqua land cover type yearly l3 global 0.05deg cmg v061 [data set]. NASA EOSDIS Land Processes Distributed Active Archive Center. doi:10.5067/MODIS/MCD12C1.061.

Fu, X., Liang, L., Ma, W., et al., 2024. EHFE refinement and extension for variable physical Earth radiation in spacecraft uncertainty thermal analysis. J. Phys: Conf. Ser. 2746 (1), 012018. https://doi.org/10.1088/1742-6596/2746/1/012018.

González-Bárcena, D., Bermejo-Ballesteros, J., Pérez-Grande, I. et al., 2022a. Selection of time-dependent worst-case thermal environmental conditions for low earth orbit spacecrafts. Adv. Space Res., 70(7), 1847–1868. URL: https://www.sciencedirect.com/science/article/pii/S0273117722005452. doi:10.1016/j.asr.2022.06.060.

González-Bárcena, D., Fernández-Soler, A., González-Llana, A. et al. (2022b). Ascent phase thermal analysis of long duration balloons. Acta Astronaut., 195, 416–429. URL: https://www.sciencedirect.com/science/article/pii/S0094576522001205. doi:10.1016/j.actaastro. 2022.03.022.

González-Bárcena, D., Fernández-Soler, A., Pérez-Grande, I. et al., 2020. Real data-based thermal environment definition for the ascent phase of polar-summer long duration balloon missions from esrange (sweden). Acta Astronaut., 170, 235–250. URL: https://www.sciencedirect.com/science/article/pii/S0094576520300357. doi:10.1016/j.actaastro.2020.01.024.

González-Bárcena, D., Sanz-Andres, A., Perez-Grande, I., et al., 2021. The worst-case thermal environment parameters of small satellites based on real-observation data. In: 50th International Conference on Environmental Systems.

González-Llana, A., González-Bárcena, D., Pérez-Grande, I. et al., 2018. Selection of extreme environmental conditions, albedo coefficient and earth infrared radiation, for polar summer long duration balloon missions. Acta Astronaut., 148, 276–284. URL: https://www.sciencedirect.com/science/article/pii/S0094576518304132. doi:10.1016/j.actaastro.2018.05.016.

Green, A., Peyrou-Lauga, R., 2015. Using real earth albedo and earth ir flux for spacecraft thermal analysis. In: 29th European Space Thermal Analysis Workshop (pp. 19–50).

Gueymard, C.A., 2018. A reevaluation of the solar constant based on a 42-year total solar irradiance time series and a reconciliation of spaceborne observations. Solar Energy, 168, 2–9. doi:10.1016/j.solener.2018.04.001. Advances in Solar Resource Assessment and Forecasting.

Hakuba, M.Z., Reynerson, C.M., Quadrelli, M.B., et al., 2024. Modeling radiation pressure accelerations: Earth radiance anisotropy, spacecraft shape and global sampling. In: 2024 IEEE Aerospace Conference, pp. 1–7. https://doi.org/10.1109/AERO58975.2024.10521289.

Iqbal, M., 1983. An introduction to solar radiation. Academic Press Canada.

Justus, C., Batts, G., Anderson, B., et al., 2001. Simple Thermal Environment Model (STEM) User's Guide. Technical Report NASA/TM-2001-211222 Marshall Space Flight Center.

Knocke, P.C., Ries, J.C., Tapley, B.D., 1988. Earth radiation pressure effects on satellites. Astrodynamics Conference. https://doi.org/10.2514/6.1988-4292, URL: https://arc.aiaa.org/doi/abs/10.2514/6.1988-4292.

Loeb, N., Su, W., Doelling, D. et al., 2018. 5.03 - earth's top-of-atmosphere radiation budget. In: S. Liang (Ed.), Comprehensive Remote Sensing (pp. 67–84). Oxford: Elsevier. URL: https://www.sciencedirect.com/science/article/pii/B9780124095489103677. doi:10.1016/B978-0-12-409548-9.10367-7.

Michalsky, J.J., 1988. The astronomical almanac's algorithm for approximate solar position (1950–2050). Sol. Energy 40 (3), 227–235. https://doi.org/10.1016/0038-092X(88)90045-X.

NASA/LARC/SD/ASDC, 2017. CERES and GEO-Enhanced TOA, Within-Atmosphere and Surface Fluxes, Clouds and Aerosols Daily Terra-Aqua Edition4A. doi:10.5067/Terra+Aqua/CERES/SYN1degDay_L3.004A.

NGA.STND.0036_1.0.0_WGS84, 2014. National Geospacial-Intelligence Agency (NGA) Standardization Document, Department of Defense World Geodetic System 1984, Its Definition and Relationships with Local Geodetic Systems. URL: https://nsgreg.nga.mil/doc/view?i=4085.

Pachler, N., del Portillo, I., Crawley, E.F., et al., 2021. An updated comparison of four low earth orbit satellite constellation systems to provide global broadband. In: 2021 IEEE International Conference on Communications Workshops (ICC Workshops), pp. 1–7. https://doi.org/10.1109/ICCWorkshops50388.2021.9473799.

Panczak, T.D., Welch, M.J., Johnson, D.A. et al., 2020. TD Suite Manual For Thermal Desktop®, TD Direct®, and SINDA/FLUINT Version 6.2 Patch 2. C&R Technologies Inc.

Paul, M., 1978. Recurrence relations for integrals of associated legendre functions. Bulletin Geodesique 52 (3), 177–190. https://doi.org/10.1007/BF02521771.

Peyrou-Lauga, R., 2017a. A proposition for updating the environmental standards using real earth albedo and earth ir flux for spacecraft thermal analysis. In: 31th European Space Thermal Analysis Workshop, pp. 19–32.

Peyrou-Lauga, R., 2017b. Using real earth albedo and earth ir flux for spacecraft thermal analysis. In: 47th International Conference on Environmental Systems.

Peyrou-Lauga, R., 2022. An enhanced earth infrared flux and albedo model based on real data. In: 51st International Conference on Environmental Systems.

Reynerson, C.M., Hakuba, M., 2023. Real-time modeling of albedo pressure on spacecraft and applications for improving trajectory estimation and earth's energy imbalance measurements. In: In AIAA SCITECH 2023 Forum. https://doi.org/10.2514/6.2023-2207.

Sanad, I., Vali, Z., Michelson, D.G., 2020. Statistical classification of remote sensing satellite constellations. In: 2020 IEEE Aerospace Conference, pp. 1–15. https://doi.org/10.1109/AERO47225.2020.9172299.

Sen, Z., 2004. Solar energy in progress and future research trends. Prog. Energy Combust. Sci., 30(4), 367–416. URL: https://www.sciencedirect.com/science/article/pii/S0360128504000139. doi: 10.1016/j.pecs.2004.02.004.

Shankar, M., Loeb, N.G., Smith, N., et al., 2023. Evaluating the radiometric performance of the clouds and the earth's radiant energy system (ceres) instruments on terra and aqua over 20 years. IEEE Trans. Geosci. Remote Sens. 61, 1–11. https://doi.org/10.1109/TGRS.2023.3330398.

Smith, G.L., Rutan, D.A., 2003. The diurnal cycle of outgoing longwave radiation from earth radiation budget experiment measurements. J. Atmos. Sci., 60(13), 1529–1542. URL: https://journals.ametsoc.org/view/journals/atsc/60/13/2997.1.xml. doi:10.1175/2997.1.

Smith, G.L., Wong, T., McKoy, N., et al., 1997. Clouds and the Earth's Radiant Energy System (CERES) Algorithm Theoretical Basis Document, Grid Single Satellite Fluxes and Clouds and Compute Spatial Averages (Subsystem 6.0). Technical Report CERES ATBD Subsystem 6.0 - Grid Fluxes and Compute Spatial Averages. Release 2.2 (2).

Spencer, J.W., 1971. Fourier series representation of the position of the sun. Search 2 (5), 172.

Stephens, G.L., Campbell, G.G., Haar, T.H.V., 1981. Earth radiation budgets. J. Geophys. Res.: Oceans, 86(C10), 9739–9760. URL: https://agupubs.onlinelibrary.wiley.com/doi/abs/10.1029/JC086iC10p09739. doi: 10.1029/JC086iC10p09739.

Su, W., Corbett, J., Eitzen, Z. et al., 2015a. Next-generation angular distribution models for top-of-atmosphere radiative flux calculation from ceres instruments: methodology. Atmospheric Measurement Techniques, 8(2), 611–632. URL: https://amt.copernicus.org/articles/8/611/2015/. doi:10.5194/amt-8-611-2015.

Su, W., Corbett, J., Eitzen, Z. et al., 2015b. Next-generation angular distribution models for top-of-atmosphere radiative flux calculation from ceres instruments: validation. Atmospheric Measurement Techniques, 8(8), 3297–3313. URL: https://amt.copernicus.org/articles/8/3297/2015/.

Suttles, J.T., Green, R.N., Minnis, P. et al., 1988. Angular radiation models for Earth-atmosphere system. volume 1: Shortwave radiation. Technical Report NASA Reference Publication 1184.

Suttles, J.T., Green, R.N., Smith, G.L. et al. (1989). Angular radiation models for earth-atmosphere system. Volume 2: Longwave radiation. Technical Report NASA Reference Publication 1184, Vol. II.

Vallado, D.A., McClain, W.D., 2013. Fundamentals of Astrodynamics and Applications. Microcosm Press and Springer, Hawthorne, CA.

Vielberg, K., Kusche, J., 2020. Extended forward and inverse modeling of radiation pressure accelerations for leo satellites. J. Geodesy 94 (43). https://doi.org/10.1007/s00190-020-01368-6.

Wielicki, B.A., Barkstrom, B.R., Harrison, E.F., et al., 1996. Clouds and the Earth's Radiant Energy System (CERES): An Earth Observing System Experiment. Bull. Am. Meteorol. Soc. 77 (5), 853–868. https://doi.org/10.1175/1520-0477(1996)077<0853:CATERE>2.0.CO;2.

Zhang, T., Stackhouse, P.W., Macpherson, B., et al., 2021. A solar azimuth formula that renders circumstantial treatment unnecessary without compromising mathematical rigor: Mathematical setup, application and extension of a formula based on the subsolar point and atan2 function. Renew. Energy 172, 1333–1340. https://doi.org/10.1016/j.renene.2021.03.047.